

Deep support vector machine for PolSAR image classification

^aOnuwa Okwuashi, onuwaokwuashi@gmail.com

^{b,c}Christopher E. Ndehedehe, c.ndehedehe@griffith.edu.au

^dDupe Nihinlola Olayinka, nihinolayinka@yahoo.co.uk

^aAniekan Eyoh, aniekaneyoh@gmail.com

^aHosanna Attai, hosannaattai@gmail.com

^aDepartment of Geoinformatics and Surveying, University of Uyo, P.M.B 1017, Uyo, Nigeria

^bAustralian Rivers Institute, Griffith University, Nathan, Queensland 4111, Australia

^cSchool of Environment & Science, Griffith University, Nathan, Queensland 4111, Australia

^dDepartment of Surveying & Geoinformatics, University of Lagos, Nigeria

Abstract

The main problem posed by Polarimetric Synthetic Aperture Radar (PolSAR) image classification in remote sensing is the ability to develop classifiers that can substantially discern the different classes inherent in natural and man-made targets. Emphasis has shifted from the use of conventional classifiers to modern non-parametric classifiers such as the Artificial Neural Network (ANN) and Support Vector Machine (SVM); and most recently the hybrid Deep Neural Network (DNN) which is a fusion of Deep Learning (DL) and ANN. This research therefore presents the novel application of Deep Support Vector Machine (DSVM) which is a fusion of DL and SVM to PolSAR image classification. Two PolSAR images of Flevoland region in Netherlands, and Winnipeg in Canada are used as test beds for the experiment. The Lee filter is used to filter the images to suppress the speckle noise in the images. The Pauli decomposition is applied to decompose the images into $|S_{HH} + S_{VV}|$, $|S_{HH} - S_{VV}|$, $|S_{HV}|$ polarimetric channels. Then the Gray Level Co-occurrence Matrix (GLCM) texture feature for $|S_{HH} + S_{VV}|$, $|S_{HH} - S_{VV}|$, $|S_{HV}|$ are extracted based on correlation, contrast, energy, and homogeneity statistics, using GLCM directions 0° , 45° , 90° , and 135° with an offset distance of 60. To enhance the efficiency of the model 8, 16, 32, 64, 128, and 256 quantization levels are explored. The DSVM classifier is implemented with four kernel function: Exponential Radial Basis Function (ERBF), Gaussian Radial Basis Function (GRBF), neural, and polynomial. The first set of results is a comparison of the DSVM and SVM. The result of Flevoland image for ERBF, GRBF, neural, and polynomial kernels are 99.17 (73.39), 99.32 (74.62), 98.64 (71.28), and 99.34 (77.21) respectively; for the Winnipeg image for ERBF, GRBF, neural, and polynomial kernels are 98.65 (72.68), 98.67 (73.54), 98.27 (70.15), and 99.46 (75.03) respectively. The second set of results is a comparison of DSVM, SVM, DNN, Gaussian Mixture Model (GMM), K Nearest Neighbour (KNN), and K Means (KM) classifiers; the results for Flevoland image for DSVM, SVM, DNN, GMM, KNN, and KM are 99.12, 74.13, 96.29, 75.06, 75.85, and 21.43 respectively; while the results for Winnipeg image for DSVM, SVM, DNN, GMM, KNN, and KM are 98.76, 72.85, 95.64, 73.20, 73.91, and 25.60 respectively. Since the Kappa coefficient is presumed to be a more accurate measure for accuracy estimation, it is used to evaluate the performances of all the models. The computed Kappa coefficients for of DSVM, SVM, DNN, GMM, KNN, and KM for Flevoland are 92.45, 70.71, 88.76, 68.59, 68.62, and 18.89 respectively; while the computed Kappa coefficients for DSVM, SVM, DNN, GMM, KNN, and KM for Winnipeg are 92.45, 70.71, 88.76, 68.59, 68.62, and 18.89 respectively. Based on the metrics used to evaluate the performances of the experiments; the results show that the DSVM outperformed the other classifiers. The high accuracy obtained with the DSVM shows it is a state-of-the-art algorithm for PolSAR image classification and a significant progress in the latest of DL applications.

Keywords: Remote sensing; PolSAR image; deep support vector machine; gray level co-occurrence matrix; image classification

1. Introduction

Polarimetric Synthetic Aperture Radar (PolSAR) is an enhanced version of the basic Synthetic Aperture Radar (SAR) system; by transmitting and receiving in multiple polarizations it can better discern unique and distinct features of natural and man-made targets (Chen *et al.*, 2014; Shang *et al.*, 2019; Ferreira *et al.* 2021). The advent of PolSAR data has immensely improved remote sensing application to land cover mapping because it can present different polarizations for different characteristics of land surfaces that are vital for the categorisation of the different land cover types (Reisi-Gahrouei *et al.* 2019; Imani, 2021). PolSAR transmits and receives electromagnetic waves in diverse polarimetric states and thereby able to deliver high-resolution remotely sensed imagery in all weather conditions (Coelho *et al.*, 2018; Liu *et al.*, 2021). PolSAR images have wide range applications in mapping natural and man-made targets, for example, land cover and land use, topography, oceanography, geology, forestry, oil spill, flooding, urban change etc. (Wurm *et al.*, 2017; Sui *et al.*, 2018; Gui *et al.* 2021). PolSAR images are degraded by speckle noise caused by coherent imaging mechanism that affects the discrimination of the classes of the target (Mahdianpari *et al.*, 2019; Yahia *et al.*, 2021). The PolSAR images also have a complex data format when compared with the single polarization SAR images (Du *et al.*, 2015; Ferreira *et al.*, 2021). These drawbacks make the classification of PolSAR images extremely cumbersome (Zhang, 2008; Zhou *et al.*, 2016; Wang *et al.*, 2021). The classification of PolSAR images is usually challenging (Han *et al.*, 2020; Parikh *et al.*, 2020; Shang *et al.*, 2020; Gopal Singh *et al.*, 2021). To overcome these challenges, many prominent machine learning algorithms like Artificial Neural Network (ANN), Support Vector Machine (SVM), K Means (KM), K Nearest Neighbour (KNN), Gaussian Mixture Model (GMM), Ensemble Learning (EL), Linear Discriminative Laplacian Eigenmaps (LDLE) have been applied to PolSAR image classification (Attarchi, 2020; Parikh *et al.*, 2020; Wang *et al.*, 2021).

The processing of the PolSAR image commences from the despeckling of the image using speckle filters (Mullissa *et al.*, 2021). The scalar and adaptive filters are basically the two categories of speckle filters (Joel & Sivakumar, 2013). The scalar filters include the mean and median filters. In the mean filter the pixel value is replaced by the mean value of the intensity of the pixels in the mask window (Gonzales & Woods, 2002); while in the median filter the centre pixel is replaced by the median value of all the pixels (Loupas *et al.*, 1989). The mean and median filters hence yield a less blurring image and therefore preserve the image edges. Prominent adaptive filters include Lee, Frost, Kuan, and Weiner filters. The Lee filter is based on the multiplicative speckle model capable of using local statistics to preserve edges and features. Lee filter achieves image denoising by lowering the variance over the image area (Lee, 1980; Lee, 1981). In the Frost filter, a weighted sum of the values within the moving kernel is replaced by the pixel of interest with a weighted sum of the values. The Frost filter being an adaptive and exponentially-weighted averaging filter is based on the coefficient of variation, which can be expressed as the ratio of the local standard deviation to the local mean of the noisy image. The Frost filter assumes the multiplicative noise and stationary noise statistics such that the weighting factors decrease with distance from the pixel of interest. In order words, the weighting factors increase for the central pixels as variance within the kernel increases (Frost *et al.*, 1982). The Kuan filter transforms multiplicative model into signal dependent additive model and thereafter applies the minimum mean square criterion to the model (Kuan *et al.*, 1985). The Wiener filter denoises the image by minimising the error between the estimated signal and the ideal signal. Wiener filter denoises the image by computing the local image variance. The efficiency of the Wiener filter increases when the computed local variance of the image is large, and its efficiency decreases when the computed local variance is small (Wiener, 1949; Jain, 1989; Gonzalez & Woods, 2008).

Polarimetric decomposition is a common method of extracting information from the PolSAR data. Before texture features are extracted from PolSAR images they are decomposed into different polarimetric channels (Ponnuramam & Rao, 2018; Shi *et al.*, 2021). PolSAR images can be used to map the environment through measurements of polarimetric properties of natural and man-made scatters (Nguyen *et al.*, 2021; Ramya & Kumar, 2021). PolSAR imaging uses the scattering matrix to identify the scattering behaviour of real-world objects after their interaction with the electromagnetic wave. This scattering matrix is represented by a combination of horizontal and vertical polarization states of transmitted and received signals (Mahdianpari *et al.*, 2018). To process the PolSAR image, this scattering matrix is decomposed into smaller components. This process of decomposing PolSAR images is called “polarimetric decomposition.” The decomposition of the scattering matrix can be done using notable PolSAR decomposition methods. There are coherent and incoherent methods of decomposition. Examples of coherent decomposition methods are Pauli decomposition, Krogager decomposition, and Cameron decomposition. Examples of incoherent decomposition methods are Freeman decomposition, Phenomenological Huynen decomposition, and eigenvector-eigenvalue based decomposition (An *et al.*, 2011; Ahishali *et al.*, 2021).

The products of polarimetric decomposition are images used by texture models to derive statistical vector data of the PolSAR image (Kourgli *et al.*, 2012; Liu *et al.*, 2021; Zhai *et al.*, 2021). Prominent examples of texture models are Gray Level Co-Occurrence Matrix (GLCM) (Haralick *et al.*, 1973), Laplace filters (Marr & Hildreth, 1980) and Granulometric analysis (Mering & Chopin, 2002). GLCM is a matrix that depicts different combinations of gray levels located in an image (Numbisi *et al.*, 2019). The GLCM is used to extract textures that represent different regions in the image for better image interpretation (Soh & Tsatsoulis, 1999; Özcan *et al.*, 2020). Laplace filters use a convolution to detect edges of objects in an image; typically, areas in the image with high texture with considerable high spatial frequency (Kupidura, 2019). Granulometric analysis is based on a classical sequence of opening and closing operations that measure the differences between successive images (Salazar *et al.*, 2020).

Using the extracted textures features, conventional parametric statistical classifiers such as KM, KNN, GMM have been used to classify PolSAR images. However, these techniques mainly rely on the supposition that the probabilities of class memberships can be modelled by a specific probability distribution function (Fränti & Sieranoja, 2018; Tavallali *et al.*, 2021). This assumption compromises the performance of the algorithm. Recent machine learning algorithms such as ANN (Rollet *et al.*, 1998; Del Frate *et al.*, 2003; Xia *et al.*, 2018; Araujo *et al.*, 2020; Linka *et al.*, 2021) and SVM (Cortes & Vapnik, 1995) have overcome this shortcoming since they are non-parametric and need no requirement for assumptions for statistical frequency distributions. These non-parametric models can yield far higher accuracies than their counterpart conventional parametric methods (Alberga *et al.*, 2008; McNairn *et al.*, 2009; Waske & Braun, 2009). Traditional classifiers such as KM, KNN, GMM have been applied to PolSAR image classification. Gadhiya and Roy (2019) proposed a fast PolSAR image classification algorithm that utilised the global KM algorithm and the superpixel-driven optimized Wishart network. KM was crucial for deriving the optimal cluster centres within each class. Richardson *et al.* (2010) applied the KNN graph technique for PolSAR image classification. This technique was used to resolve the nonlinear structures inherent in a typical PolSAR data. Gao *et al.* (2014) applied a complex GMM and Wishart mixture model for land cover classification of PolSAR Images from the RADARSAT-2 sensor of the Canadian Space Agency (CSA), the AIRSAR sensor of the Jet Propulsion Laboratory (JPL), and the EMISAR sensor of the Technical University of Denmark (DTU). Because of the complexity of PolSAR images contemporary classifiers like Artificial Neural Network (ANN) and Support Vector Machine (SVM) top the list of contemporary classifiers proven to be robust for SAR image classification. Hara *et al.* (1994) applied the ANN to PolSAR image classification. The results were compared to those of the conventional methods. The results showed that the ANN outperformed the conventional classifiers. Fukuda and Hirose (2001) proposed an SVM based classification scheme of land cover from PolSAR data using the polarimetric feature vectors, the intensity of each channel, complex correlation coefficients and textural information were the input into the SVM. The model yielded satisfactory classification results. Rostami and Kaveh (2021) introduced a hybrid biogeography-based optimization SVM to classify PolSAR images of RADARSAT 2 in band C acquired from San Francisco, USA, by feature minimization to maximize classification accuracy. Three steps were implemented: pre-processing, feature selection and classification. It was found that the proposed method outperformed other algorithms.

Current trends in machine learning have demonstrated significant improvement in classification accuracy by integrating Deep Learning (DL) and contemporary classifiers (Lussier *et al.*, 2020; Kotsiopoulos *et al.*, 2021). In recent times DL has revolutionised image classification/pattern recognition (Milošević *et al.*, 2020; Shao *et al.*, 2021). The fusion of DL and ANN is largely called “Deep Neural Network (DNN).” The DNN has been highly effective in PolSAR image classification than the traditional ANN (Liu *et al.*, 2018; Zhang *et al.*, 2018; Shen *et al.*, 2020; Boulila *et al.*, 2021). Zhou *et al.* (2016) investigated the efficacy of Deep Convolutional Neural Network (DCNN) in supervised classification of PolSAR images of San Francisco, USA and Flevoland, The Netherlands. The model outputs were significantly improved. Geng *et al.* (2017) applied Deep Supervised and Contractive Neural Network (DSCNN) for PolSAR image classification. The texture features were extracted using GLCM, Gabor, and histogram of oriented gradient descriptors. The model yielded improved classification performance when compared with related known techniques. Chen and Tao (2018) implemented the classification of PolSAR image using polarimetric feature driven DCNN. The new model incorporated expert knowledge of target scattering mechanism interpretation and polarimetric feature mining to assist the polarimetric feature driven DCNN in achieving both training efficiency and classification accuracy. Classical roll-invariant polarimetric features and hidden polarimetric features in the rotation domain were used to improve the robustness of the new model. They found that the proposed model outperformed the convolutional ANN model. Ma and Zhu (2019) presented a novel land cover classification scheme for a PolSAR image using the Convolutional Neural Network (CNN) and superpixel. The new model used both the intensity and phase information to determine the label of each pixel based on the inherent spatial relations. Then the superpixel generating algorithm is used to determine the superpixel representation of Pauli decomposition image as well as the contour information that showed the boundary of each category. The final map label is a fusion of the original label map and contour information. The new model was able to accomplish enhanced performance by correcting label misclassification. Shang *et al.*

(2020) proposed a new network, the densely connected and Depthwise Separable convolutional Neural network (DSNet) for PolSAR image classification to improve the performance of the traditional CNN. The DSNet model achieved better results when compared with the traditional method on three different datasets. They inferred that apparently, conventional methods such as the CNN are restricted because they do not consider the spatial neighbourhood information that may lead to the misclassification of target labels. Ahishali *et al.* (2021) implemented the classification of PolSAR images using compact CNNs. The proposed method helped to mitigate the problem of “curse of dimensionality” by applying a compact and adaptive implementation of CNNs using a sliding-window classification approach. The advantages of the new model are: (i) there was no need for an extensive feature extraction procedure (ii) computational efficiency (iii) the model required a smaller window size to implement classification. The model achieved a range between 92.33–99.39% classification accuracy.

Notably, DL frameworks are emerging as more sophisticated routines and PolSAR observations have necessitated new DL hybrid methods. The deep learning techniques so far applied to PolSAR image classification are ANN based. Therefore, in the quest for improving PolSAR image classification accuracy, this work seeks to experiment a novel integration of DL and SVM, called “Deep Support Vector Machine” (DSVM) for PolSAR image classification. The input into the DSVM will be the extracted feature vectors obtained from the GLCM via Pauli decomposition. The concept of DSVM is new, evolving, and at its infancy. The application of the hybrid DSVM for hyperspectral image classification has recently been demonstrated by Okwuashi and Ndehedehe (2020), highlighting its efficacy as a state-of-the art routine, amongst other DL hybrid formations. While spectral information can directly be used for hyperspectral image classification, the PolSAR image cannot easily be classified using direct spectral data because it is often degraded by speckles present in the image and also its complex data nature. It is expected that PolSAR image classification will pose a considerable challenge when compared to hyperspectral image classification. We argue that overcoming this challenge requires the decomposition of the PolSAR image and the textural extraction of the PolSAR image features. The hybrid DSVM imitates the DNN that consists of numerous hidden layers. The numerous hidden layers are connected by series of weights, which are replaced by several SVM functions being initialised with the SVM regularisation parameter. The optimal DSVM is outputted by updating the connecting SVM functions in the hidden layer. GLCM being a renowned feature texture model has found application in several PolSAR image applications. More recently, Parida and Mandal (2020) retrieved the textural measures from a decomposed ALOS L-band PolSAR image in Western parts of Mizoram, Northeast India using the GLCM. Here, we present for the first time the classification of PolSAR imagery using Deep Support Vector Machine (DSVM) based on Gray Level Co-occurrence Matrix (GLCM) texture feature. Two PolSAR images of Flevoland regions in Netherlands and Winnipeg in Canada are used as experimental test beds for this study. To assess the robustness of the hybrid DSVM model, its results are compared against those of the SVM, DNN, GMM, KNN, and KM.

2. Models

2.1 Filtering, image decomposition and texture feature extraction models

2.1.1 Lee filter

Lee filter is based on the minimum square error criterion that uses the local statistics technique. By applying the Lee filter the speckle noise is reduced while the edges in the image are preserved. The Lee filter reduces the speckle noise by applying a spatial filter to every pixel using the following formula,

$$LF = L_M + K * (P_C - M * L_M). \quad (1)$$

Where $K = M * L_V / ((L_M * L_M * MV(M * M * L_V)))$ and $MV = 1/NLooks$. PC is the centre pixel value of window. L_M is the local mean of filter window. L_V is the local variance of filter window. M is the multiplicative noise mean. MV is the multiplicative noise variance. $NLooks$ is the number of looks (Lee, 1980; Lee, 1981).

2.1.2 Pauli decomposition

Pauli decomposition is one the methods used to analyse coherent targets. Coherent decomposition handles the decomposition of the scattering matrix, while incoherent decomposition handles the decomposition of the covariance matrices. Pauli decomposition is used to extract the polarisation characteristics of objects (Wei *et al.*, 2014; Zhai *et al.*, 2021). The polarimetric information in a single SAR image in the measured complex scattering matrix $[S]$ using Pauli decomposition is expressed as a linear combination of the scattering responses of simpler objects (Zhang *et al.*, 2008; Imani, 2021). Pauli decomposition represents the measure of scattering in the Pauli

basis, considering an orthogonal linear (H,V) basis (Liu *et al.*, 2021). The Pauli basis $\{[S]_A, [S]_B, [S]_C, S_D\}$ can be expressed by the following 2 X 2 matrices,

$$[S]_A = \frac{1}{\sqrt{2}} \begin{bmatrix} 1 & 0 \\ 0 & 1 \end{bmatrix} \quad (2)$$

$$[S]_B = \frac{1}{\sqrt{2}} \begin{bmatrix} 1 & 0 \\ 0 & -1 \end{bmatrix} \quad (3)$$

$$[S]_C = \frac{1}{\sqrt{2}} \begin{bmatrix} 0 & 1 \\ 1 & 0 \end{bmatrix} \quad (4)$$

$$[S]_D = \frac{1}{\sqrt{2}} \begin{bmatrix} 0 & -1 \\ 1 & 0 \end{bmatrix} \quad (5)$$

Using matrices 2, 3, and 4 the Pauli basis can be reduced to basis,

$$\{[S]_A, [S]_B, [S]_C\} \quad (6)$$

Therefore, a given scattering matrix $[S]$ can be expressed as,

$$[S] = \begin{bmatrix} S_{HH} & S_{HV} \\ S_{VH} & S_{VV} \end{bmatrix} = \alpha [S]_A + \beta [S]_B + \gamma S_C \quad (7)$$

Where,

$$\alpha = \frac{S_{HH} + S_{VV}}{\sqrt{2}} \quad (8)$$

$$\beta = \frac{S_{HH} - S_{VV}}{\sqrt{2}} \quad (9)$$

$$\alpha = \sqrt{2} S_{HV} \quad (10)$$

From equations 8, 9, and 10 the SPAN of $[S]$ can be written as,

$$\text{SPAN} = |S_{HH}|^2 + |S_{VV}|^2 + 2|S_{HV}|^2 = |\alpha|^2 + |\beta|^2 + |\gamma|^2 \quad (11)$$

The polarimetric information of $[S]$ is expressed by simply the combination of intensities

$|S_{HH}|^2$, $|S_{VV}|^2$, and $2|S_{HV}|^2$ in a single image Red-Green-Blue (RGB) image, though the most used codification of RGB is normally expressed in terms of equations 12, 13, and 14 as,

$$|\alpha|^2 = \text{Red} \quad (12)$$

$$|\beta|^2 = \text{Green} \quad (13)$$

$$|\gamma|^2 = \text{Blue} \quad (14)$$

Pauli decomposition can yield a colour image to visualise PolSAR data based on the three primary scattering mechanisms. By introducing a vector K , Pauli decomposition can be described as,

$$K = [S_{HH} + S_{VV} \quad S_{HH} - S_{VV} \quad 2S_{HV}]. \quad (15)$$

Where K denotes coherent polarimetric vector, S_{HH} , S_{HV} , S_{VH} , S_{VV} are the complex backscattering coefficients of the four polarised channels. The representation in a RGB image is given as: Red = $|S_{HH} + S_{VV}|$, Green = $|S_{HH} - S_{VV}|$, and Blue = $|S_{HV}|$ (Aghababaei *et al.*, 2013).

2.1.3 Gray level co-occurrence matrix

GLCM was introduced by Haralick *et al.* (1973). GLCM is a matrix that represents the distribution of co-occurring grayscale levels in an image at a given offset (Haralick *et al.*, 1973; Khojastehnazhand & Ramezani, 2020). The GLCM is a statistical method of depicting the texture of an image by considering the spatial relationship of the image pixels (Delibaş & Arslan, 2020). The GLCM is a second order statistical tool used for characterising the texture of an image (Zhang *et al.*, 2020; Khan *et al.*, 2021). These statistical measures are extracted from the image by characterising the texture of the image based on the calculation of pairs of a pixel with specific values and a specified relationship reoccurring in an image. The GLCM is calculated by recording how often pairs of pixel with specific values and in a specified spatial distance occur within an image. We can create the GLCM for an image with p pixel values, therefore the $p \times p$ GLCM G can be defined over an $n \times m$ image I with an offset Δx , Δy as,

$$G_{\Delta x \Delta y}(i, j) = \sum_{i=1}^n \sum_{j=1}^m \begin{cases} 1, & \text{if } I(x, y) = i \text{ and } I(x + \Delta x, y + \Delta y) = j \\ 0, & \text{otherwise} \end{cases} \quad (16)$$

Where i and j denote the pixel values, x and y represent the spatial positions in the image I , the offsets $(\Delta x, \Delta y)$ represent the spatial relation for which the matrix is calculated, and $I(x, y)$ represent the pixel value at pixel (x, y) . The operation of the GLCM can be simplified by simply applying the distance d and an angle θ instead of an offset $(\Delta x, \Delta y)$. The resulting GLCM is,

$$GCLM = \begin{bmatrix} p(0,0) & p(0,1) & \cdot & \cdot & \cdot & p(0,N-1) \\ p(1,0) & p(1,1) & \cdot & \cdot & \cdot & p(1,N-1) \\ \cdot & \cdot & & & & \cdot \\ \cdot & \cdot & & & & \cdot \\ \cdot & \cdot & & & & \cdot \\ p(N-1,0) & p(N-1,1) & \cdot & \cdot & \cdot & p(N-1,N-1) \end{bmatrix} \quad (17)$$

Our PolSAR image is an 8 bit image (2^8) that can store 256 (0-255) possible colours or gray levels. The GLCM describes the conditional joint probabilities of all pairwise combinations of the gray levels (i, j) restricted by inter-pixel distance or offset distance d and orientation θ in an $n \times n$ spatial window. The common four angular orientations of the GLCM are p_0 , p_{45} , p_{90} , and p_{135} ($\theta = 0^\circ, 45^\circ, 90^\circ, 135^\circ$) (Figure 1). The distances of these angular orientations are given as the following,

$$\begin{aligned} \theta = 0^\circ : & \Leftrightarrow [0 \ d] \Leftrightarrow 0 \ 1; 0 \ 2; 0 \ 3; 0 \ 4; \cdot \ \cdot \ \cdot \\ \theta = 45^\circ : & \Leftrightarrow [-d \ d] \Leftrightarrow -1 \ 1; -2 \ 2; -3 \ 3; -4 \ 4; \cdot \ \cdot \ \cdot \\ \theta = 90^\circ : & \Leftrightarrow [-d \ 0] \Leftrightarrow -1 \ 0; -2 \ 0; -3 \ 0; -4 \ 0; \cdot \ \cdot \ \cdot \\ \theta = 135^\circ : & \Leftrightarrow [-d \ -d] \Leftrightarrow -1 \ -1; -2 \ -2; -3 \ -3; -4 \ -4; \cdot \ \cdot \ \cdot \end{aligned}$$

Figure 1 shows the spatial relationships of pixels defined by the array of offsets. Figure 2a is first order image, while Figures 2b, 2c, 2d, 2e are second order images. Given a hypothetical 2-bit (2^2) image with quantization level of 4 (0-3 gray levels) (Figure 2a), let us compute the GLCM for $\theta = 0^\circ, 45^\circ, 90^\circ$, and 135° (Figure 2). For 0° (Figure 2b) in the first row there are three instances of the (0,0) therefore its value is 3. There are no instances of (0,1), (0,2), and (0,3) therefore their value is 0. Row 2 to row 4 were computed in like manner. For 45° (Figure 2c) in the first row there are two instances of (0,0) therefore its value is 2. There are one instance of (0,1) therefore its value is 1. There are no instances of (0,2) and (0,3). Row 2 to row 4 were computed in like manner. For 90° (Figure 2d) in the first row there two instances of (0,0) therefore its value is 2. There are two instances of (0,1) therefore its value is 2. There are no instances of (0,2) and (0,3) therefore their values are both 0. Row 2 to row 4 were computed in like manner. For 135° (Figure 2e) in the first row there is one instance of (0,0) therefore

its value is 0. There are two instances of (0,1) therefore its value is 2. There are no instances of (0,2), and (0,3) therefore their values are both 0. Row 2 to row 4 were computed in like manner.

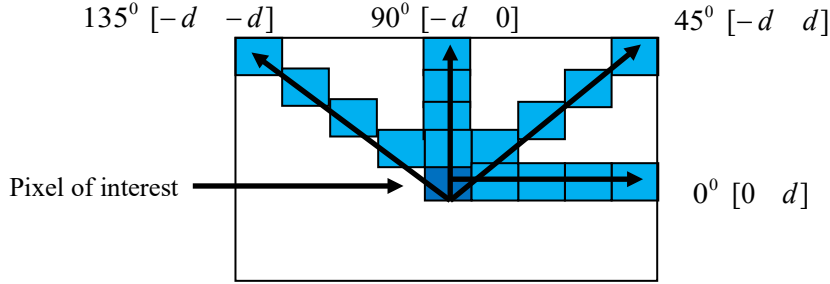


Figure 1: Spatial relationship of pixels and array of offsets.

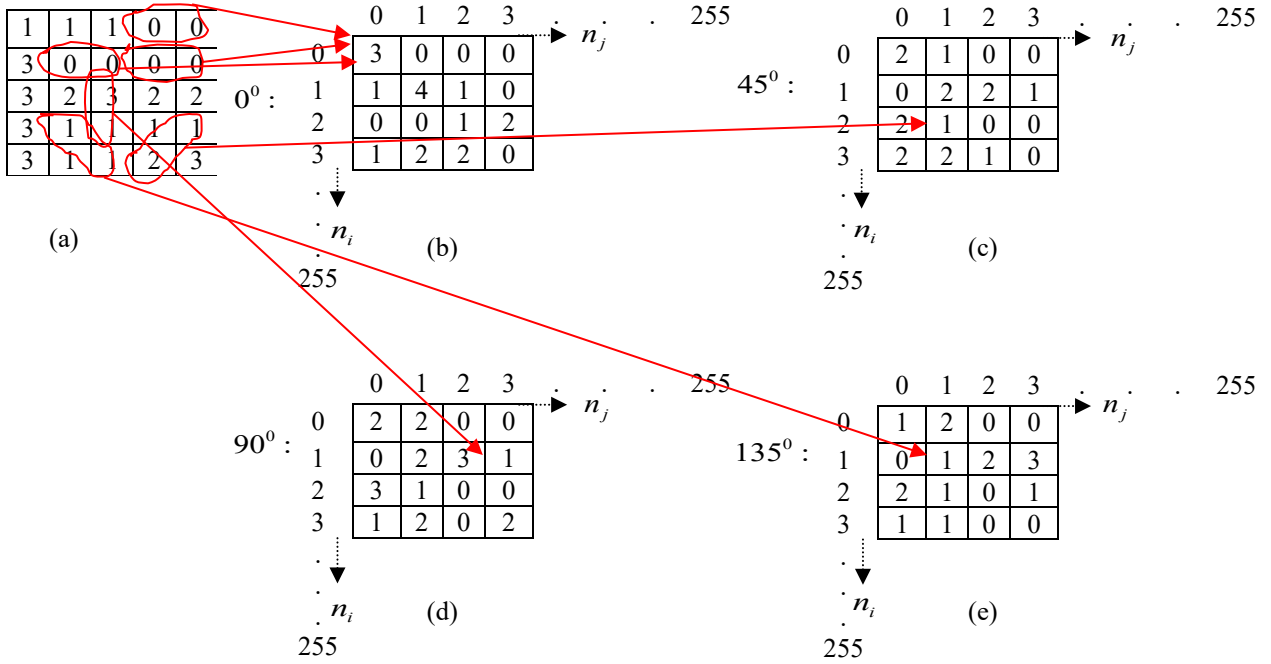


Figure 2: Illustration on how to compute the GLCM: (a) hypothetical image (b) 0° GLCM (c) 45° GLCM (d) 90° (e) 135° GLCM.

The following statistics were used to extract vector data from the computed GLCM: (i) correlation (ii) contrast (iii) energy, and (iv) homogeneity,

$$Correlation = \sum_{i=0}^{N-1} \sum_{j=0}^{N-1} \frac{(i - \mu_i)(j - \mu_j)p(i, j)}{\sigma_i \sigma_j}, \quad (18)$$

where $\mu_i = \sum_j i \sum_j p(i, j)$, $\sigma_i = \sum_i (i - \mu_i)^2 \sum_j p(i, j)$, $\mu_j = \sum_j j \sum_i p(i, j)$,

and $\sigma_j = \sum_j (j - \mu_j)^2 \sum_i p(i, j)$.

$$Contrast = \sum_{i=0}^{N-1} \sum_{j=0}^{N-1} (i-j)^2 p(i, j) \quad . \quad (19)$$

$$Energy = \sum_{i=0}^{N-1} \sum_{j=0}^{N-1} p^2(i, j) \quad . \quad (20)$$

$$Homogeneity = \sum_{i=0}^{N-1} \sum_{j=0}^{N-1} \frac{p(i, j)}{1 + (i-j)^2} \quad . \quad (21)$$

The correlation measures the joint probability occurrence of the specified pixel pairs with a range of $[-1 \ 1]$. The correlation returns a measure of how correlated each pixel is with its neighbours. The contrast also known as variance and inertia measures the local variations in the gray level co-occurrence matrix with a range of $[0 \ (\text{size}(\text{GLCM},1)-1)^2]$. The contrast returns a measure of the intensity of contrast between each pixel and its neighbours. Energy also known as uniformity or the angular second moment computes the sum of squared elements in the GLCM with a range $[0 \ 1]$. Energy returns a measure of the sum of squared elements in the GLCM. Homogeneity measures the closeness of the distribution of the GLCM elements to the GLCM diagonal with a range of $[0 \ 1]$. Homogeneity returns the measure of the closeness of how the elements in the GLCM are distributed with respect to the GLCM diagonal (Wang *et al.*, 2020). For computational efficiency and enhancement in classification accuracy our original 8-bit (2^8) image (0-255) gray levels can be quantized to other levels; this process is called quantization. The quantization level for (0-255 gray levels) is 256. Our 8-bit image can be quantized to 7-bit (2^7) (0-127), 6-bit (2^6) (0-63), 5-bit (2^5) (0-31), 4-bit (2^4) (0-15), and 3-bit (2^3) (0-7) images. The quantization levels for 7-bit, 6-bit, 5-bit, 4-bit, and 3-bit images are 128, 64, 32, 16 and 8 respectively. The size of the computed GLCM is equal to the quantization level of the image. For example Figure 2a is an image of (0-3) gray levels, therefore its quantization level is 4 because it consists of four elements 0, 1, 2, and 3. Automatically a 4 X 4 GLCM image (Figure 2b) will be computed from Figure 2a. Conventionally 8, 16, 32, 64, 128, 256 quantization levels are usually used in remote sensing image classification.

2.2 Deep support vector machine model

Given a binary problem that the training set has n -training samples, that is, $(x_1, y_1), (x_2, y_2), \dots, (x_n, y_n)$, where $x_i \in \mathfrak{R}^N$ is an N dimensional vector that belongs to one of classes $y_i \in \{-1, +1\}$ SVM will classify this binary problem using a linear hyperplane (Cortes & Vapnik, 1995; Guyon *et al.*, 2002; Maulik & Chakraborty, 2017; Pirra & Diana, 2019). The given binary classification problem can be separated using a linear decision function,

$$f(x) = w \cdot x + b \quad (22)$$

where $w \in \mathfrak{R}^N$ denotes a vector that determines the orientation of the desired hyperplane required for the separation, and $b \in \mathfrak{R}$ is the bias. The optimal hyperplane required to separate the two objects is,

$$y_i(w \cdot x + b) \geq 1 \quad (23)$$

By solving the following constrained optimization problem or primal problem, the solution to this problem can be found,

$$\text{minimise } \frac{1}{2} w \cdot w + C \sum_{i=1}^n \xi_i \quad (24)$$

subject to: $y_i(w \cdot x + b) \geq 1 - \xi_i$, $\xi_i > 0$, and for $\forall i = 1, \dots, n$; where C , $0 < C < \infty$, is the penalty value or regularisation parameter; while ξ_i are the slack variables (Zendehboudi *et al.*, 2018). For a nonlinear case the optimisation problem is given as,

$$\text{maximise } \sum_{i=1}^n \alpha_i - \frac{1}{2} \sum_{i=1}^n \sum_{j=1}^n \alpha_i \alpha_j y_i y_j K(x_i, x_j) \quad (25)$$

subject to: $\sum_{i=1}^n \alpha_i y_i = 0$, and, $0 \leq \alpha_i \leq C$, for $i = 1, \dots, n$. The resulting decision function is,

$$f(x) = \text{sign} \left[\sum_{i=1}^n y_i \alpha_i^0 K(x_i, x) + b^0 \right]. \quad (26)$$

α_i^0 is the support vector and $K(x_i, x)$ is the kernel function or kernel trick (Okwuashi & Ndehedehe, 2017). DSVM can be created by using a multi-layer architecture with multiple hidden layers (Figure 3).

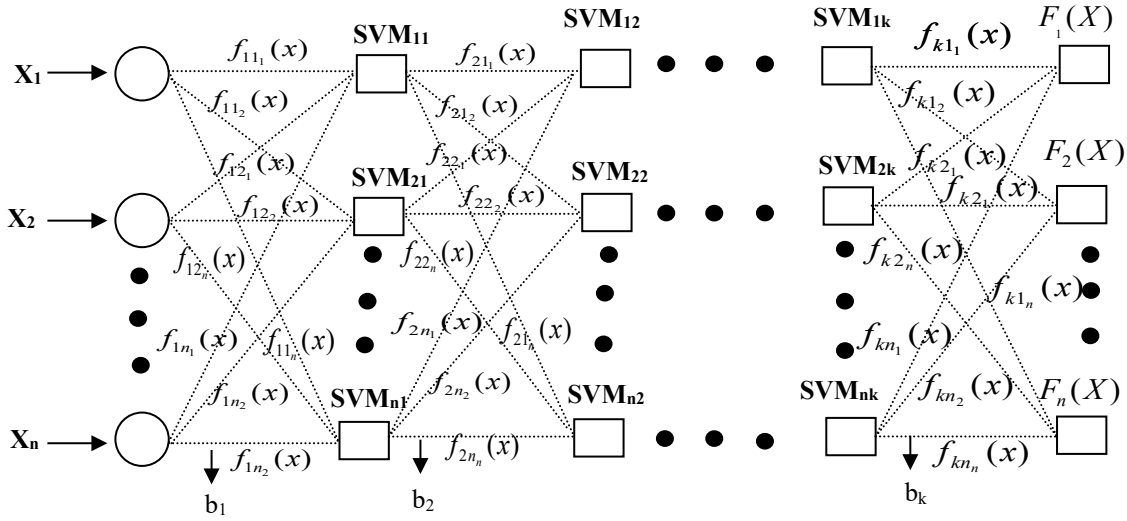


Figure 3: Architecture of the DSVM.

X_1, X_2, \dots, X_n are the input layer data points. The multiple hidden layers consist $SVM_{11}, SVM_{12}, \dots, SVM_{1k}, SVM_{21}, SVM_{22}, \dots, SVM_{2k}$, and $SVM_{n1}, SVM_{n2}, \dots, SVM_{nk}$; while $F_1(X), F_2(X), \dots, F_n(X)$ denote the output layer points. For X_1 , the output for training $SVM_{11}, SVM_{12}, \dots, SVM_{1k}$ is $F_1(X)$. For X_2 , the output for training $SVM_{21}, SVM_{22}, \dots, SVM_{2k}$ is $F_2(X)$. For X_n , the output for training $SVM_{n1}, SVM_{n2}, \dots, SVM_{nk}$ is $F_n(X)$. The network weights are represented as $f(x)$. All the various $f(x)$ are evaluated in the hidden layers, which are multiple layers that connect all the input neurons with the output neurons. The total net input to each hidden layer neuron can be expressed as,

$$\begin{aligned} net_{h1} &= f_{11_1}(x) \cdot X_1 + f_{11_2}(x) \cdot X_2 + \dots + f_{11_n}(x) \cdot X_n + b1 \\ net_{h2} &= f_{12_1}(x) \cdot X_1 + f_{12_2}(x) \cdot X_2 + \dots + f_{12_n}(x) \cdot X_n + b1 \\ &\vdots \\ net_{hn} &= f_{1n_1}(x) \cdot X_1 + f_{1n_2}(x) \cdot X_2 + \dots + f_{1n_n}(x) \cdot X_n + b1 \end{aligned} \quad (27)$$

The logistic activation function is used to compute the output for each input neuron as,

$$\begin{aligned}
out_{h1} &= \frac{1}{1 + e^{-net_{h1}}} \\
out_{h2} &= \frac{1}{1 + e^{-net_{h2}}} \\
&\bullet \\
&\bullet \\
&\bullet \\
out_{hn} &= \frac{1}{1 + e^{-net_{hn}}}
\end{aligned} \tag{28}$$

The output of the hidden layer neurons are used as input to compute the output layer neurons $net_{o1}, \dots, net_{o1_n}$, $net_{o2_1}, \dots, net_{o2_n}$, and $net_{on_1}, \dots, net_{on_n}$ as,

$$\begin{aligned}
net_{o1_1} &= f_{21_1}(x) \cdot out_{h1} + f_{21_2}(x) \cdot out_{h2} + \dots + f_{21_n}(x) \cdot out_{hn} + b_2 \\
&\bullet \\
&\bullet \\
&\bullet
\end{aligned} \tag{29}$$

$$net_{o1_n} = f_{k1_1}(x) \cdot out_{h1} + f_{k1_2}(x) \cdot out_{h2} + \dots + f_{k1_n}(x) \cdot out_{hn} + b_2$$

$$\begin{aligned}
net_{o2_1} &= f_{22_1}(x) \cdot out_{h1} + f_{22_2}(x) \cdot out_{h2} + \dots + f_{22_n}(x) \cdot out_{hn} + b_2 \\
&\bullet \\
&\bullet \\
&\bullet
\end{aligned} \tag{30}$$

$$net_{o2_n} = f_{k2_1}(x) \cdot out_{h1} + f_{k2_2}(x) \cdot out_{h2} + \dots + f_{k2_n}(x) \cdot out_{hn} + b_2$$

$$\begin{aligned}
net_{on_1} &= f_{2n_1}(x) \cdot out_{h1} + f_{2n_2}(x) \cdot out_{h2} + \dots + f_{2n_n}(x) \cdot out_{hn} + b_k \\
&\bullet \\
&\bullet \\
&\bullet
\end{aligned} \tag{31}$$

$$net_{on_n} = f_{kn_1}(x) \cdot out_{h1} + f_{kn_2}(x) \cdot out_{h2} + \dots + f_{kn_n}(x) \cdot out_{hn} + b_k$$

For simplicity let us consider only the case of $net_{o1}, \dots, net_{o1_n}$. Its output can be computed with the logistic activation function as,

$$\begin{aligned}
out_{o1_1} &= \frac{1}{1 + e^{-net_{o1_1}}} \\
&\bullet \\
&\bullet \\
&\bullet \\
out_{o1_n} &= \frac{1}{1 + e^{-net_{o1_n}}}
\end{aligned} \tag{32}$$

The error for computing the output $output_{o1}$ for only X_1 , can be calculated by subtracting the computed output $output_{o1}$ from the known value of $F_1(X)$ as,

$$E_{o1} = \sum_{i=1}^n \frac{1}{2} (F_1(X) - \text{output}_{o1_i}) \quad (33)$$

In like manner the total error can be computed by summing all the computed errors $E_{o1}, E_{o2}, \dots, E_{on}$ as,

$$E_{total} = E_{o1} + E_{o2} + \dots + E_{on}. \quad (34)$$

By applying the method of backpropagation we can update each $f(x)$ in the network so that they will ensure that the actual output becomes closer to the target output $F(X)$, thereby minimising the error for each of the output neurons as well as the entire network. For example, $f_{11_1}(x)$ can be computed as the gradient of ∂E_{total} as,

$$\frac{\partial E_{total}}{f_{11_1}(x)} = \frac{\partial \text{net}_{o1_1}}{\partial f_{11_1}(x)} * \frac{\partial \text{out}_{o1_1}}{\partial \text{net}_{o1_1}} * \frac{\partial E_{total}}{\partial \text{out}_{o1_1}} \quad (35)$$

The updated function $f_{11}^{(new)}(x)$ can be computed as,

$$f_{11_1}^{(new)}(x) = f_{11_1}(x) - \lambda * \frac{\partial E_{total}}{\partial f_{11_1}(x)} \quad (36)$$

Where λ denotes the learning rate for adjusting the weights of the network. In like manner all the weights in the network that is $f(x)$ will be updated and the process will be repeated iteratively from equation 12 until E_{total} becomes zero or infinitesimal (Okwuashi & Ndehedehe, 2020).

3. Implementation

The first experiment was an L-band fully PolSAR image of Flevoland region in Netherlands, obtained by AIRSAR system of NASA laboratory in 1989. The SAR image has a resolution of range and azimuth of 6.7m and 12.1m respectively, and scene size of 750 X 1024 pixels. It is a farmland PolSAR data that consist of 11 classes as follows: water, forest, wheat, rapeseed, beet, grassland, potato, alfalfa, bare land, stem bean, and pea. The Pauli RGB image and Ground truth are shown in Figures 4a and 4b.

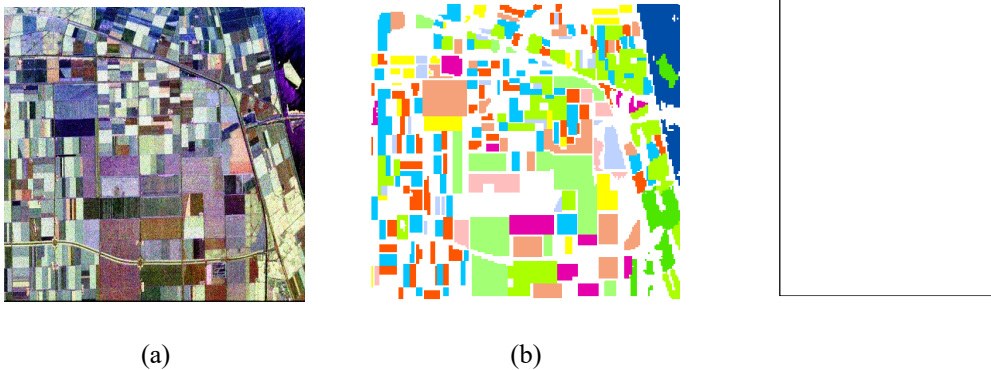


Figure 4: (a) Pauli RGB image of Flevoland. (b) Ground truth of Flevoland.

In order to suppress the speckle noise in the image, a 5 X 5 window size Lee filter was applied. The Pauli RGB image of the filtered image is shown in Figure 5. Using Pauli decomposition the image was decomposed into $|S_{HH} + S_{VV}|$, $|S_{HH} - S_{VV}|$, $|S_{HV}|$ polarimetric channels shown in Figure 6. GLCM texture features for $|S_{HH} + S_{VV}|$, $|S_{HH} - S_{VV}|$, $|S_{HV}|$ polarimetric channels were extracted for correlation, contrast, energy, and homogeneity statistics. For example the computed correlation, contrast, energy, and homogeneity statistics for $|S_{HH} + S_{VV}|$ based on directions 0° , 45° , 90° , and 135° an offset distance of 60 is shown in Figure 7, while the correlation plot for directions 0° , 45° , 90° , and 135° is shown in Figure 8.

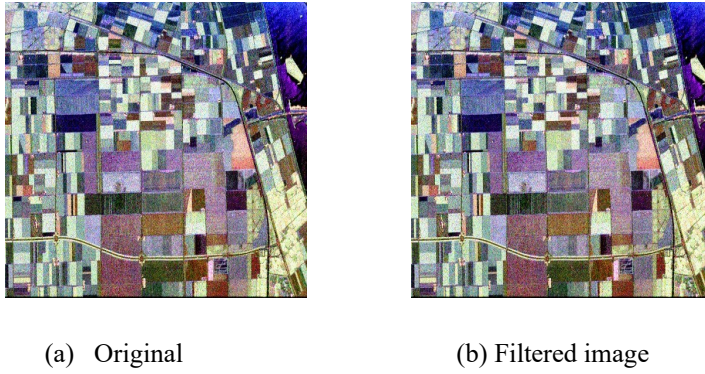


Figure 5: Pauli RGB original and filtered image of Flevoland.

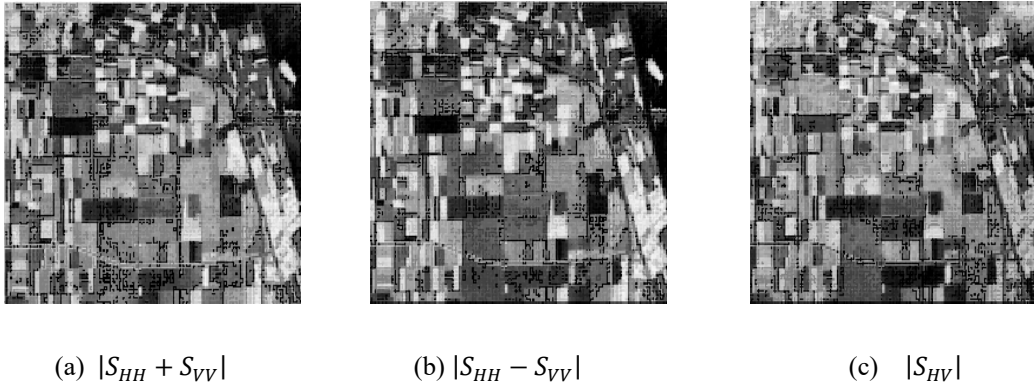


Figure 6: Flevoland images of Pauli decomposition images for $|S_{HH} + S_{VV}|$, $|S_{HH} - S_{VV}|$, $|S_{HV}|$ polarimetric channels.

From Figure 7a, there is a stronger correlation among 45° , 90° , 135° , than between 45° , 90° , 135° and 0° . The correlation decreased steadily from offset 0 to 60. This implied that the larger the offset distance among the pixels the lower the correlation among the pixels. From Figure 7b, the contrast estimated the variations in the gray levels over distance or offset. Figure 7b showed that the computed contrast of the four directions 0° , 45° , 90° , and 135° increased as the offset increases. Figure 7c showed that the energy among pixels for directions 0° , 45° , 90° , and 135° decreases as the offset increases. This implied that the pixels that are close to each other will exude higher energy. Figure 7d showed that the homogeneity among the pixels for directions 0° , 45° , 90° , and 135° decreases as the offset increases. This implied that the distribution of the elements within the diagonal of the computed GLCM is higher at low offset distances among the pixels and lower at high offset distances among the pixels.

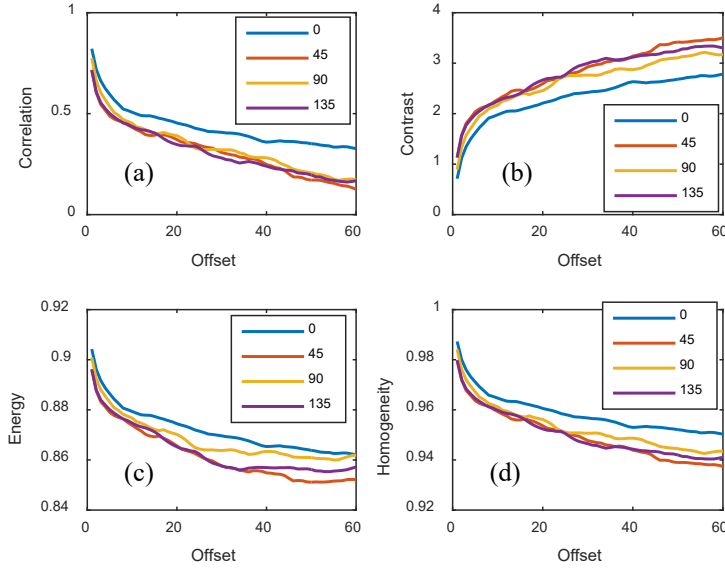


Figure 7: Correlation, contrast, energy, homogeneity versus offset at directions 0° , 45° , 90° , and 135° of Flevoland for $|S_{HH} + S_{VV}|$ polarimetric channel.

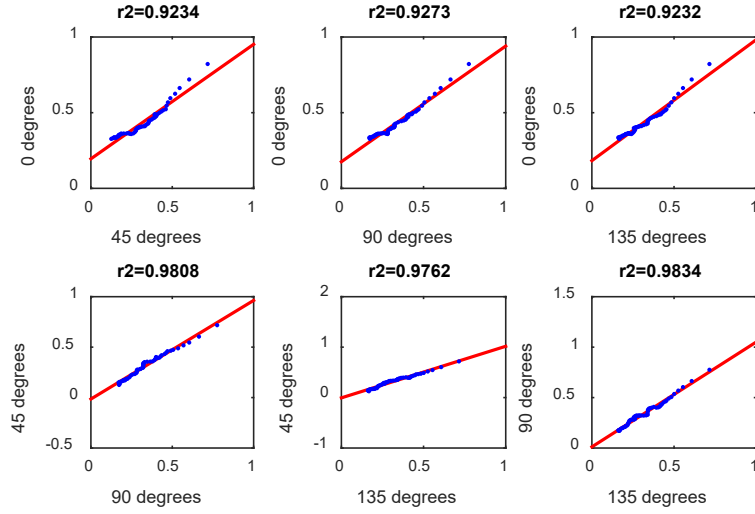


Figure 8: Correlation plot for directions 0° , 45° , 90° , and 135° of Flevoland for $|S_{HH} + S_{VV}|$ polarimetric channel.

A strong correlation is expected among directions 0° , 45° , 90° , and 135° (see Figure 8). The higher the r^2 value the stronger the correlation while the lower the r^2 value the weaker the correlation. The strongest correlation was between 90° and 135° while the weakest correlation was between 0° and 135° . From Figure 9, the four statistics were extracted based on 8, 16, 32, 64, 128, and 256 quantization levels. For correlation, there is no significant difference among the six quantization levels, but most of the data range between 0.65 and 0.82. The median value for the six quantization levels range between 0.72 and 0.74. Conclusively the different quantization levels did not have a significant impact on the correlation feature.

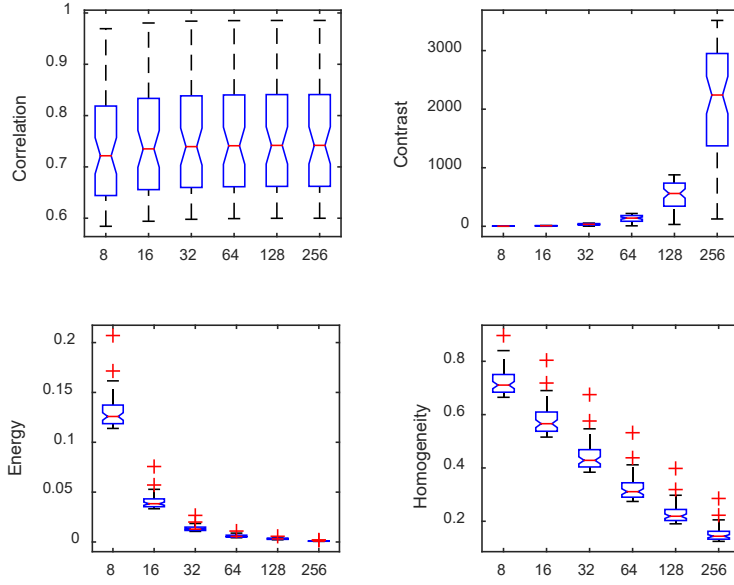


Figure 9: Box plot of 8, 16, 32, 64, 128, and 256 quantization levels for correlation, contrast, energy, and homogeneity for Flevoland.

The computed contrast increased as the quantization levels increased. This implied that the quantization levels had a significant impact on the contrast feature. The computed energy was highest at quantization level 8 but reduces steadily till quantization level 256. There was significant difference in the computed energy for all the quantization. This implied that the various levels of quantization had a significant impact in the computed energy feature. The computed homogeneity was highest at quantization level 8 but reduces steadily till quantization level 256. There was significant difference in the computed homogeneity for all the quantization. Therefore, we can conclude that the various levels of quantization had a significant impact in the computed homogeneity feature.

The second experiment is a PolSAR image which was acquired by the fully polarimetric UAVSAR system, over an agricultural area in Winnipeg, MB, Canada, in July 2012. This agricultural area consists of 6 classes as follows: oats, soybeans, wheat, broadleaf, corn, and canola. The Pauli RGB image and ground truth are shown in Figures 10a and 10b. The speckle noise in the image was suppressed by applying a 5 X 5 window size Lee Filter over the image. The Pauli RGB image of the filtered image is shown in Figure 11.

Using Pauli decomposition the image was decomposed into $|S_{HH} + S_{VV}|$, $|S_{HH} - S_{VV}|$, $|S_{HV}|$ polarimetric channels shown in Figure 12. GLCM texture features for $|S_{HH} + S_{VV}|$, $|S_{HH} - S_{VV}|$, $|S_{HV}|$ polarimetric channels were extracted for correlation, contrast, energy, and homogeneity statistics. For example the computed correlation, contrast, energy, and homogeneity statistics for $|S_{HH} + S_{VV}|$ based on directions 0° , 45° , 90° , and 135° an offset distance of 60 is shown in Figure 13, while the correlation plot for directions 0° , 45° , 90° , and 135° is shown in Figure 14.

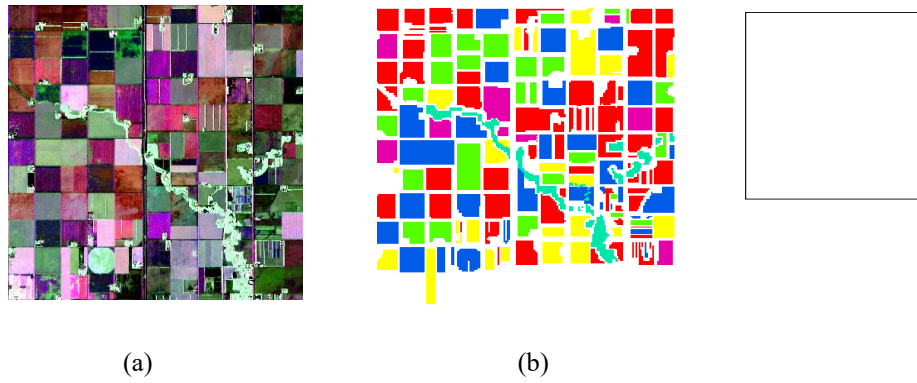


Figure 10: (a) Pauli RGB image of Winnipeg. (b) Ground truth of Winnipeg.

From Figure 13a, there is a stronger correlation among 0° , 45° , 90° , and 135° . The correlation values decreased steadily from offset 0 to 60. This implied that the larger the offset distance among the pixels the lower the correlation among the pixels. From Figure 13b, the contrast estimated the variations in the gray levels over distance or offset and the computed contrast of the four directions 0° , 45° , 90° , and 135° increased as the offset increases.

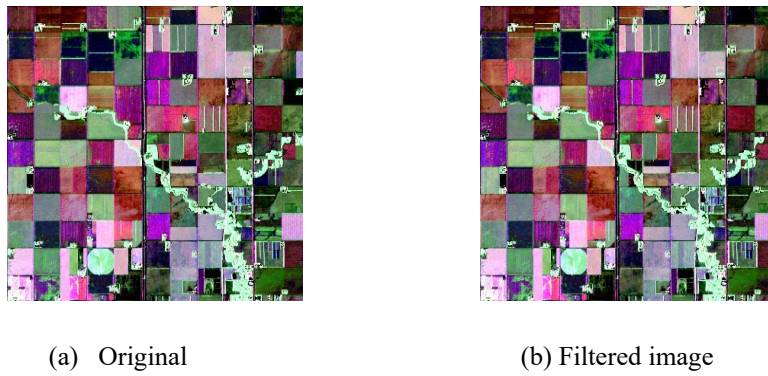


Figure 11: Pauli RGB original and filtered image of Winnipeg.

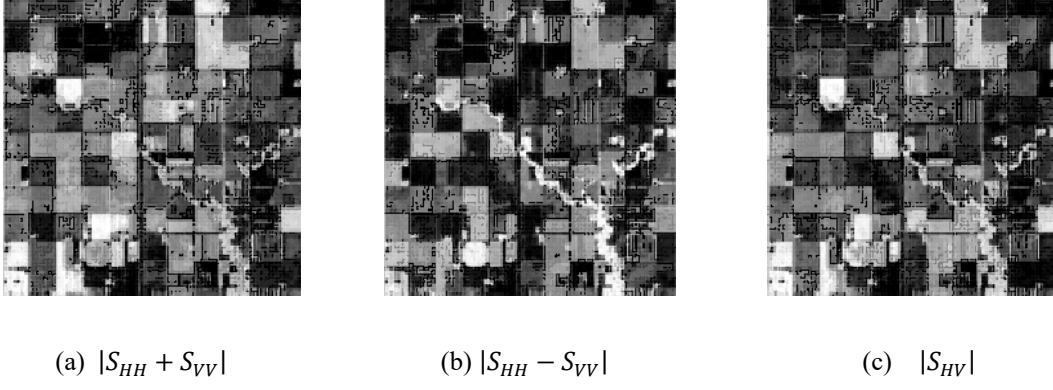


Figure 12: Winnipeg images of Pauli decomposition for $|S_{HH} + S_{VV}|$, $|S_{HH} - S_{VV}|$, $|S_{HV}|$ polarimetric channels.

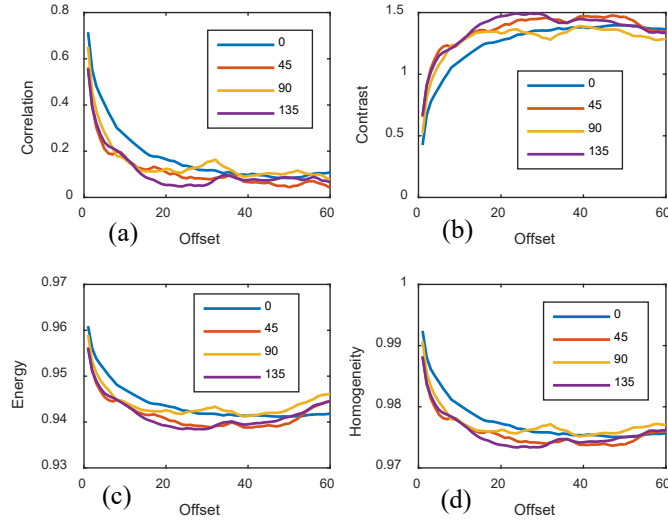


Figure 13: Correlation, contrast, energy, homogeneity versus offset at directions 0° , 45° , 90° , and 135° of Winnipeg for for $|S_{HH} + S_{VV}|$ polarimetric channel.

Figure 13c showed that the energy among pixels for directions 0° , 45° , 90° , and 135° decreases as the offset increases. This implied that the pixels that are close to each other radiated higher energy than the pixels that are far apart. Figure 13d showed that the homogeneity among the pixels for directions 0° , 45° , 90° , and 135° decreases as the offset increases. This implied that the distribution of the elements within the diagonal of the computed GLCM is higher at low offset distances among the pixels and lower at high offset distances among the pixels. It is expected that there will be a strong correlation among directions 0° , 45° , 90° , and 135° (see Figure 14).

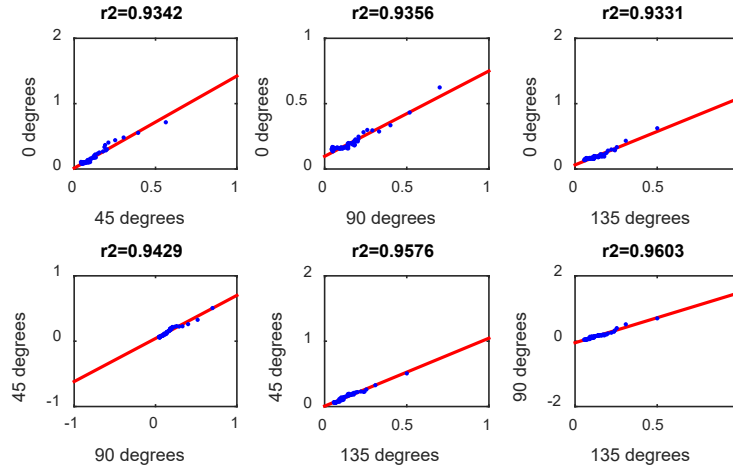


Figure 14: Correlation plot for 0, 45, 90, and 135 of Winnipeg for $|S_{HH} + S_{VV}|$ polarimetric channel.

The higher the r^2 value the stronger the correlation while the lower the r^2 value the weaker the correlation. The strongest correlation was between 90^0 and 135^0 while the weakest correlation was between 0^0 and 135^0 . From Figure 15, the four statistics were extracted based on 8, 16, 32, 64, 128, and 256 quantization levels. For correlation, there is no significant difference among the six quantization levels, but most of the data range between 0.42 and 0.63. The median value for the six quantization levels range between 0.46 and 0.47. Conclusively the different quantization levels did not have a significant impact on the correlation feature.

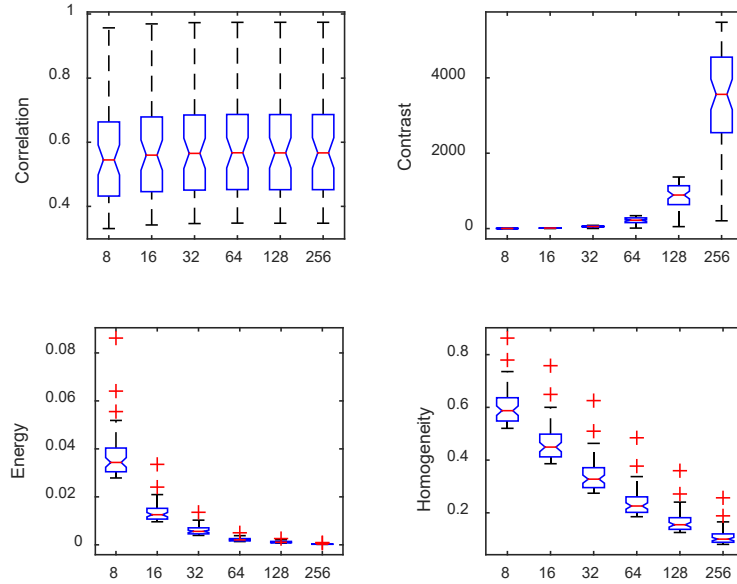


Figure 15: Box plot of 8, 16, 32, 64, 128, and 256 quantization levels for correlation, contrast, energy, and homogeneity for Winnipeg

The mean vectors of directions $\theta = 0^0, 45^0, 90^0$, and 135^0 and quantisation levels 8, 16, 32, 64, 128, and 256 were used to calculate the vectors of the correlation, contrast, energy, and homogeneity data. These four statistical texture features were fed into the DSVM model for the image classification. Tables 1 and 2 consisted of the training and test datasets for Flevoland and Winnipeg. As shown in the tables each experiment consisted of 100

different training datasets. For Flevoland 1,070 training pixels and 10,822 test pixels were selected, while for Winnipeg 1,050 training pixels and 10,814 test pixels were selected.

Table 1: Training and test sets for Flevoland.

Class	Name	Training set						Test set
		X_1	X_2	.	.	.	X_{100}	
1	Water	75	76				74	757
2	Forest	56	55				55	435
3	Wheat	101	99				102	1196
4	Potato	199	198				200	2000
5	Grassland	150	149				148	1673
6	Bareland	138	138				136	1301
7	Rapeseed	137	136				138	1359
8	Alfalfa	60	63				61	582
9	Pea	44	43				45	392
10	Stem bean	46	47				48	497
11	Beet	64	66				63	630
Total		1070	1070				1070	10822

Table 2: Training and test sets for Winnipeg.

Class	Name	Training set						Test set
		X_1	X_2	.	.	.	X_{100}	
1	Soybeans	352	354				353	3802
2	Canola	236	237				238	2423
3	Wheat	186	185				184	1788
4	Corn	147	146				148	1443
5	Oats	70	71				72	771
6	Broadleaf	59	57				55	587
Total		1050	1050				1050	10814

The learning result of the DSVM is the composite of individual SVM. Each SVM was trained using four kernel function, Exponential Radial Basis Function (ERBF) kernel $K(x_i, x_j) = \exp\left(-\frac{\|x - y\|}{2\gamma^2}\right)$, Gaussian Radial Basis

Function (GRBF) kernel $K(x_i, x_j) = \exp\left(-\frac{\|x - y\|^2}{2\gamma^2}\right)$, neural kernel $K(x_i, x_j) = \tanh(ax_i \cdot x_j + b)$, and

polynomial kernel $K(x_i, x_j) = (x_i \cdot x_j + c)^d$. Let simplicity let us compute the kernels for $f_{111}(x)$ for a 5 X 5 data,

$$x_i = \begin{bmatrix} 0.8 & 0.2 & 0.3 & 0.2 \\ 0.1 & 0.5 & 0.1 & 0.6 \\ 0.6 & 0.2 & 0.4 & 0.1 \\ 0.4 & 0.7 & 0.8 & 0.9 \\ 0.1 & 0.9 & 0.1 & 0.3 \end{bmatrix} = |A|.$$

We computed the ERBF kernel $K(x_i, x_j) = \exp\left(-\frac{\|x - y\|}{2\gamma^2}\right)$, given that $\gamma = 0.4$ as,

$$K\left\langle \exp\left(-\frac{\|x-y\|^2}{2\gamma^2}\right)\right\rangle = \exp\{-(A[A]^T)/2 \times 0.4^2\} = \begin{bmatrix} 0.08 & 0.36 & 0.13 & 0.06 & 0.34 \\ 0.36 & 0.14 & 0.44 & 0.04 & 0.13 \\ 0.13 & 0.44 & 0.17 & 0.08 & 0.38 \\ 0.06 & 0.04 & 0.08 & 0 & 0.04 \\ 0.34 & 0.13 & 0.38 & 0.04 & 0.06 \end{bmatrix}$$

We computed the GRBF kernel $K(x_i, x_j) = \exp\left(-\frac{\|x-y\|^2}{2\gamma^2}\right)$, given that $\gamma = 0.8$ as,

$$K\left\langle \exp\left(-\frac{\|x-y\|^2}{2\gamma^2}\right)\right\rangle = \exp\{-(A[A]^T)^2/2 \times 0.8^2\} = \begin{bmatrix} 0.19 & 0.25 & 0.25 & 0.05 & 0.22 \\ 0.25 & 0.21 & 0.30 & 0.05 & 0.17 \\ 0.25 & 0.30 & 0.30 & 0.08 & 0.27 \\ 0.05 & 0.05 & 0.08 & 0 & 0.04 \\ 0.22 & 0.17 & 0.27 & 0.04 & 0.14 \end{bmatrix}$$

We computed the neural kernel $K(x_i, x_j) = \tanh(ax_i \cdot x_j + b)$, given that $a = 0.2$ and $b = 0.4$ as,

$$K(\tanh[ax_i \cdot x_j + b]) = \tanh(0.2 \times [A][A]^T + 0.4) = \begin{bmatrix} 0.51 & 0.44 & 0.49 & 0.52 & 0.44 \\ 0.44 & 0.48 & 0.42 & 0.54 & 0.49 \\ 0.49 & 0.42 & 0.47 & 0.51 & 0.43 \\ 0.52 & 0.54 & 0.51 & 0.68 & 0.54 \\ 0.44 & 0.49 & 0.43 & 0.54 & 0.53 \end{bmatrix}.$$

We computed the neural kernel $K(x_i, x_j) = (x_i \cdot x_j + c)^d$, given that $c = 0$ and $d = 2$ as,

$$K(x_i \cdot x_j + c)^d = ([A][A]^T + 0)^2 = \begin{bmatrix} 2.10 & 1.76 & 1.80 & 3.77 & 1.92 \\ 1.76 & 2.02 & 1.53 & 3.92 & 2.23 \\ 1.80 & 1.53 & 1.55 & 3.27 & 1.67 \\ 3.77 & 3.92 & 3.27 & 7.87 & 4.29 \\ 1.92 & 2.23 & 1.67 & 4.29 & 2.53 \end{bmatrix}.$$

The output label of the SVM was labelled -1 and +1. The binary SVM was modified to a multi-class classifier by adopting the One Against All (OAA) technique. The OAA modifies a binary classifier for multi-class classification by classifying each of the classes of interest against the remaining classes. The OAA is one of the most widely applied methods of extending binary classifiers to multi-class problems. Our hybrid DSVM was designed to mimics the DNN in operation. Individual SVMs were constructed to function as interconnecting weights of the network. The results were compared against the target or output $F(X)$ based on the backpropagation technique. One hundred distinct inputs X_1, X_2, \dots, X_{100} were used to obtain one hundred distinct outputs. Starting with an initial weight with labels +1 and -1 for $f_{11_1}(x)$, Tables 1 and 2 showed some of the results of the updated weights of $f_{11_1}(x)$ and some of the predicted results of $F_1(X)$ for Flevoland and Winnipeg images. Hence the initial weights of the network for $f_{11_1}(x)$, $f_{11_2}(x)$, $f_{12_1}(x)$, $f_{12_2}(x)$, ..., $f_{kn_n}(x)$, were initialised using the regularisation parameter values $0 \leq C \leq \infty$. The next was the training of the network by the method of backpropagation, that simply updates the weights in the network $f(x)$. Since the DSVM process is an iteration process, an error function or loss function $E = \sum \frac{1}{2}(F(X) - \text{output})$ was used to determine when the iteration converges. Conventionally the learning of the network terminates when the loss function is zero or infinitesimal. With regards the computational cost of any algorithm that solves the SVM problem when considering arbitrary kernel matrices the two systemic complexities involved are the training and testing time.

Generically the experimental results would indicate that the training set will have a smaller running time than the testing set. The reality is that characterisation of the time complexity of the DSVM is fairly intricate in running a traditional SVM time and space complexity are linear with respect to the outputted number of support vectors.

Considering that the asymptotical number of support vectors grows linearly with the number of examples, the computational cost of solving the SVM problem realistically has both a quadratic and a cubic component.

For each SVM we selected the optimal parameter values based on a cross-validation procedure for ERBF, GRBF, neural, and polynomial kernels for Flevoland and Winnipeg images as shown in Figures 16 and 17. The optimal parameter values for these kernels are the parameter value with the least error value. Since it is impossible to present the results of all the SVMs, let us present the results for $f_{11_1}(x)$. For Flevoland, the optimal gamma values for ERBF and GRBF kernels were 0.4 and 0.2 respectively. The optimal parameter values for the neural kernel were 0.2 and 0.4 for a and b respectively. The optimal parameter values for the polynomial kernel were 3 and 4 for c and d respectively.

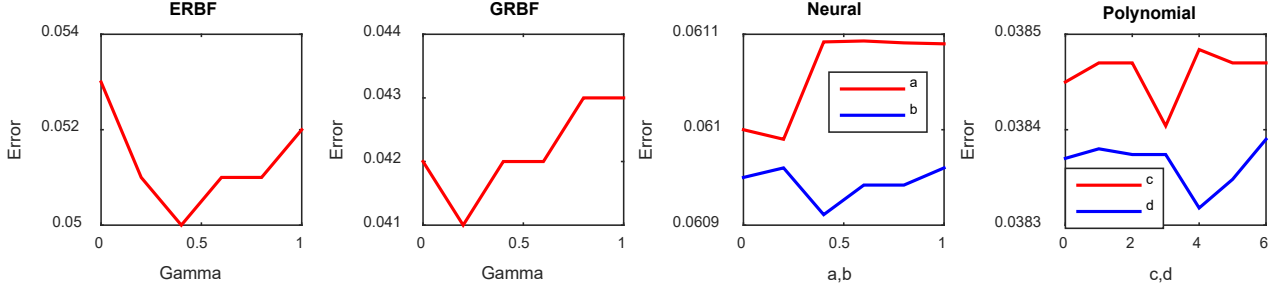


Figure 16: Selection of optimal model parameter values for ERBF, GRBF, neural, and polynomial kernels for Flevoland

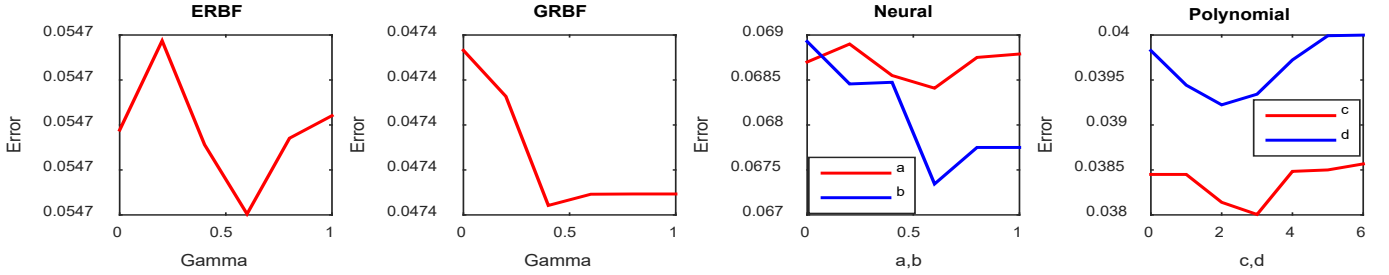


Figure 17: Selection of optimal model parameter values for ERBF, GRBF, neural, and polynomial kernels for Winnipeg

For the Winnipeg image the optimal gamma values for ERBF and GRBF kernels were 0.6 and 0.4 respectively. The optimal parameter values for the neural kernel were both 0.6 for a and b respectively. The optimal parameter values for the polynomial kernel were 2 and 3 for c and d respectively.

For each SVM we selected the optimal C values based on a cross-validation procedure for ERBF, GRBF, neural, and polynomial kernels for Flevoland and Winnipeg images as shown in Figures 18 and 19 respectively. The optimal C values for these kernels are the values with the least error value. Since it is impossible to present the results of all the SVMs, let us present the results for $f_{11_1}(x)$. The optimal C value for ERBF, GRBF, neural, and polynomial kernels was 100 for Flevoland and Winnipeg images.

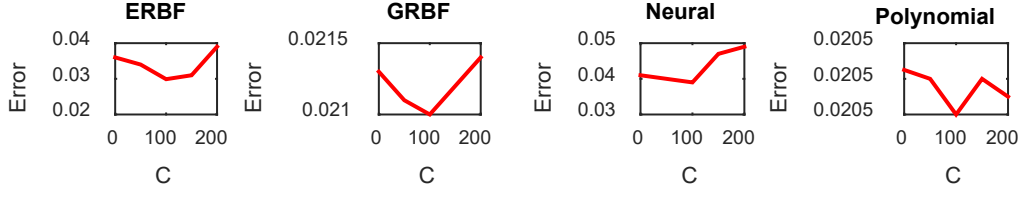


Figure 18: Selection of optimal C values for ERBF, GRBF, neural, and polynomial kernels for Flevoland

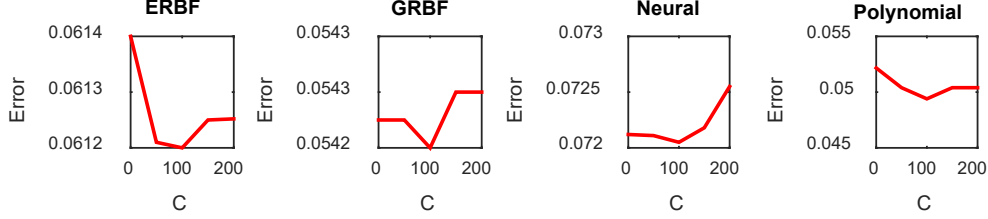


Figure 19: Selection of optimal C values for ERBF, GRBF, neural, and polynomial kernels for Winnipeg

Tables 3 and 4 contained the DSVM training and test results for Flevoland and Winnipeg. From Tables 3 and 4 classes +1 and -1 represent two distinct binary classes for $f_{11_1}(x)$ and $f_{21_1}(x)$. The support vectors resulting from $f_{11_1}(x)$ (1) and $f_{21_1}(x)$ (1) are the non-zero values, and the predicted values for each support vector must be +1.0000 and -1.0000, while the non - support vectors will yield values other than +1.0000 and -1.0000 such as +2.2842,..., -0.5817.... The updated results of $f_{11_1}(x)$ (1) and $f_{21_1}(x)$ (1) were $f_{11_1}(x)$ (2) and $f_{21_1}(x)$ (2). From Tables 3 and 4, $F_1(x)$ (predicted) were the predictions of $F_1(x)$ (initial). The results in Tables 3 and 4 showed accurate predictions of the initial labels. In machine learning there are normally errors in prediction, therefore there is no perfect algorithm in machine learning. The resulting outputs were compared against the target or output $F(X)$ based on the backpropagation technique. One hundred distinct inputs X_1, X_2, \dots, X_{100} were used to obtain one hundred distinct outputs. Starting with an initial weight from +1 to -1 for $f_{11_1}(x), f_{21_1}(x) \dots$, the updated weights of $f_{11_1}(x), f_{21_1}(x) \dots$, and the predicted results of $F_1(X)$ were obtained. The eventual results of inputs X_1, X_2, \dots, X_{100} were $F_1(X), F_2(X), \dots, F_{100}(X)$.

Table 3: Some of the DSVM training and test results for Flevoland.

$f_{11_1}(x)$	$f_{11_1}(x)$	$f_{11_1}(x)$	$f_{11_1}(x)$...	$f_{21_1}(x)$	$f_{21_1}(x)$	$f_{21_1}(x)$	$f_{21_1}(x)$...	$F_1(X)$	$F_1(X)$
initial	support vectors	predicted (1)	predicted (2)		initial	support vectors	predicted (1)	predicted (2)		initial	predicted
+1	5.2148	+1.0000	+0.8253	...	+1	0	+5.0525	+2.6596	...	+1	+4.9432
+1	0	+2.2842	+0.0937	...	+1	0	+3.6294	+0.6400	...	+1	+2.0188
+1	3.0960	+1.0000	+3.6284	...	+1	8.2673	+1.0000	+0.8659	...	+1	+3.6173
.
.
-1	2.9267	-1.0000	-2.6028	...	-1	0	-0.2753	-1.0178	...	-1	-1.7928
-1	0	-0.5817	-1.9843	...	-1	7.0499	-1.0000	-0.9895	...	-1	-2.2206
-1	0	-1.9705	-0.1472	...	-1	0	-2.5931	-1.2686	...	-1	-1.3164
.
.
.

Table 4: Some of the DSVM training and test results for Winnipeg.

$f_{11_1}(x)$ initial	$f_{11_1}(x)$ support vectors	$f_{11_1}(x)$ predicted (1)	$f_{11_1}(x)$ predicted (2)	...	$f_{21_1}(x)$ initial	$f_{21_1}(x)$ support vectors	$f_{21_1}(x)$ predicted (1)	$f_{21_1}(x)$ predicted (2)	...	$F_1(X)$ initial	$F_1(X)$ predicted
+1	0	+6.1489	+0.5300	...	+1	8.0302	+1.0000	+5.0470	...	+1	+3.3608
+1	2.9431	+1.0000	+1.6835	...	+1	0	+3.6654	+2.5633	...	+1	+4.0372
+1	7.8164	+1.0000	+3.1248	...	+1	5.9429	+1.0000	+2.8695	...	+1	+1.7785
.
.
.
-1	1.8249	-1.0000	-2.6591	...	-1	4.0468	-1.0000	-0.8248	...	-1	-2.1364
-1	0	-5.2776	-0.2532	...	-1	0	-4.0253	-1.5930	...	-1	-1.8378
-1	3.2535	-1.0000	-0.0265	...	-1	0	-3.1487	-2.5000	...	-1	-2.9820
.
.
.

Figure 20 depicted the classification results for the Flevoland image. The overall accuracy was calculated as number of correctly classified pixels divided by the sum of the incorrectly classified pixels and the correctly classified pixels. This result was for DSVM (ERBF), DSVM (GRBF), DSVM (neural), DSVM (polynomial), GMM, SVM (ERBF), SVM (GRBF), SVM (neural), SVM (polynomial), DNN, KNN, and KM classifiers. Table 5 depicted the classification results from eleven classes: water, forest, wheat, rapeseed, beet, grassland, potato, alfalfa, bare land, stem bean, and pea for ERBF, GRBF, neural, and polynomial kernels of the DSVM. The classification accuracy for water for the four kernels was 100%. For forest, ERBF kernel yielded the highest accuracy while GRBF yielded the lowest accuracy. For wheat, the accuracy for the four kernels was 100%. For rapeseed, ERBF and GRBF yielded the highest accuracy while the neural kernel yielded the lowest accuracy. For beet ERBF and GRBF yielded the highest accuracy while the neural kernel yielded the lowest accuracy. For grassland, neural yielded the highest accuracy while GRBF yielded the lowest accuracy. For potato, neural yielded the highest accuracy while ERBF yielded the lowest accuracy. For alfalfa, ERBF and polynomial yielded the highest accuracy while neural yielded the lowest accuracy. For bare land, ERBF, neural, and polynomial yielded the highest accuracy while GRBF yielded the lowest accuracy. For stem bean, ERBF yielded the highest accuracy while neural yielded the lowest accuracy. For pea GRBF yielded the highest accuracy while neural yielded the lowest accuracy.

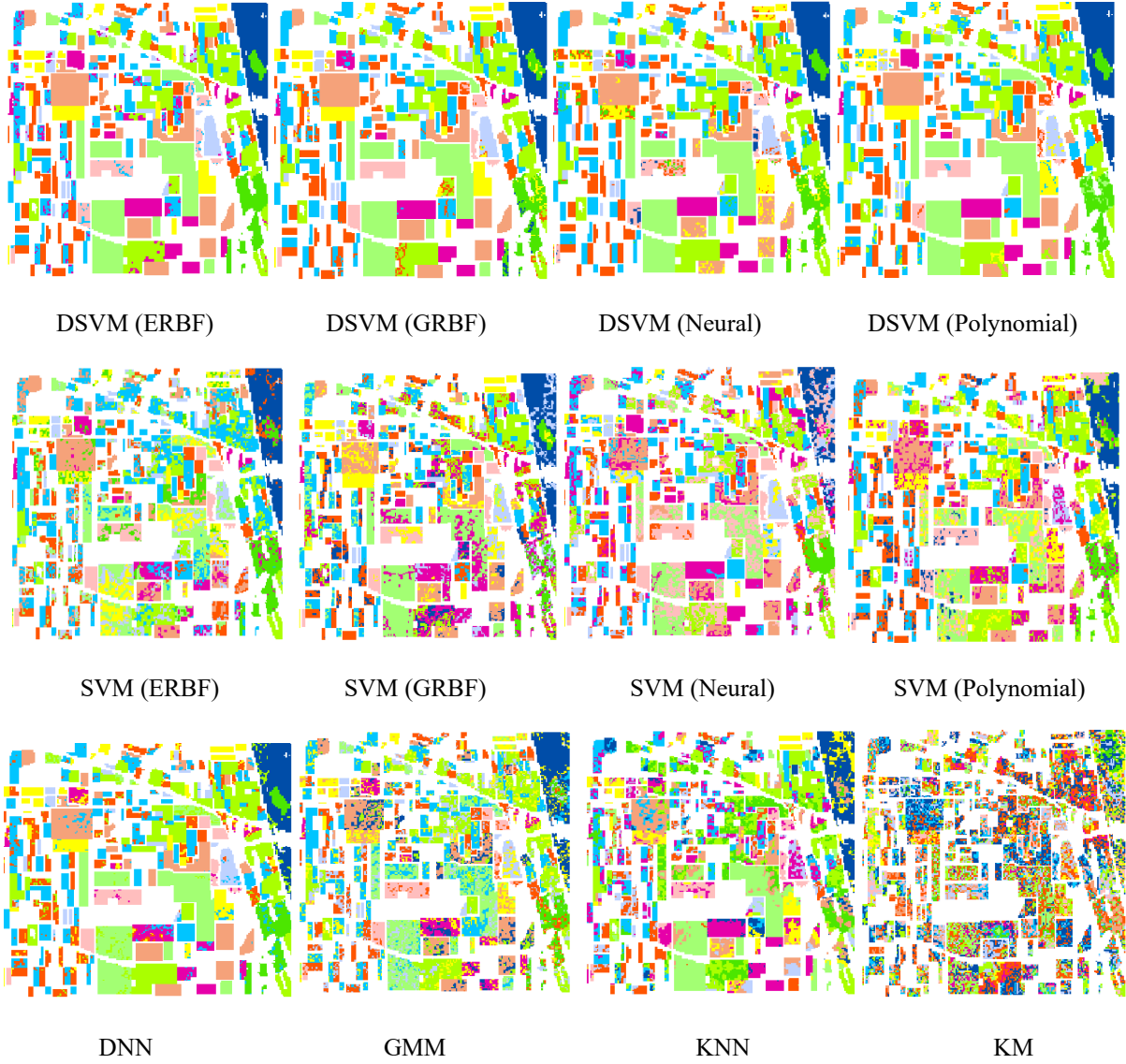


Figure 20: The classified images for Flevoland

Table 5: Classification accuracy for Flevoland for DSVM.

Class	Class name	kernels			
		ERBF	GRBF	Neural	Polynomial
1	Water	100	100	100	100
2	Forest	100	97.96	98.12	99.81
3	Wheat	100	100	100	100
4	Rapeseed	100	100	98.36	98.79
5	Beet	100	100	95.91	97.93
6	Grassland	97.99	97.28	100	98.75
7	Potato	95.03	98.46	99.93	99.14
8	Alfalfa	100	99.04	98.96	100
9	Bare land	100	99.95	100	100
10	Stem bean	99.82	99.80	98.67	99.29
11	Pea	98.05	100	95.14	99.00

Figure 21 depicted the classification results for the Winnipeg image. This result was for DSVM (ERBF), DSVM (GRBF), DSVM (neural), DSVM (polynomial), GMM, SVM (ERBF), SVM (GRBF), SVM (neural), SVM (polynomial), DNN, KNN, and KM classifiers. Table 6 depicted the classification results from six classes: oats, soybeans, wheat, broadleaf, corn, and canola for ERBF, GRBF, neural, and polynomial kernels of the DSVM. For oats, ERBF yielded the highest accuracy while neural yielded the lowest accuracy. For soybeans, polynomial yielded the highest accuracy while neural yielded the lowest accuracy. For wheat, GRBF yielded the highest accuracy while polynomial yielded the lowest accuracy. For broadleaf, polynomial yielded the highest accuracy while ERBF yielded the lowest accuracy. For corn, polynomial yielded the highest accuracy while GRBF yielded the lowest accuracy. For canola, ERBF yielded the highest accuracy while neural yielded the lowest accuracy.

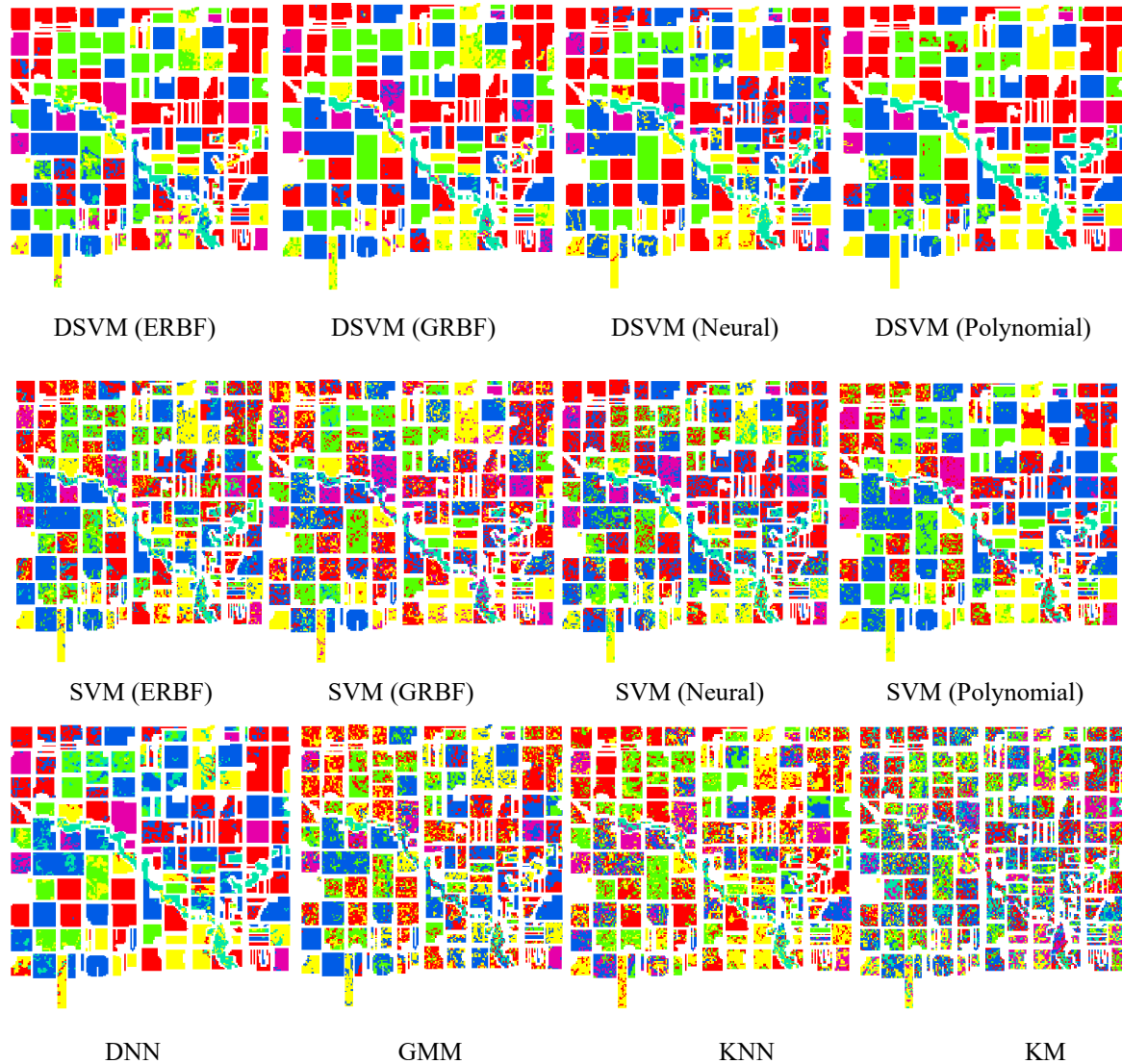


Figure 21: The classified images for Winnipeg

Table 6: Classification accuracy for Winnipeg for DSVM.

Class	Class name	kernels			
		ERBF	GRBF	Neural	Polynomial
1	Oats	100	98.48	96.20	99.56
2	Soybeans	98.76	98.89	98.75	99.11
3	Wheat	99.49	100	99.24	98.63
4	Broadleaf	95.62	98.35	99.47	99.91
5	Corn	98.13	97.80	98.25	100
6	Canola	99.89	98.51	97.68	99.57

Table 7: Comparison of the classification accuracy between DSVM and SVM (the SVM results are in parenthesis).

Images	kernels			
	ERBF	GRBF	Neural	Polynomial
Flevoland	99.17 (73.39)	99.32 (74.62)	98.64 (71.28)	99.34 (77.21)
Winnipeg	98.65 (72.68)	98.67 (73.54)	98.27 (70.15)	99.46 (75.03)

Table 8: Comparison of the classification accuracies of DSVM, SVM, DNN, GMM, KNN, and KM.

Images	Classifiers					
	DSVM	SVM	DNN	GMM	KNN	KM
Flevoland	99.12	74.13	96.29	75.06	75.85	21.43
Winnipeg	98.76	72.85	95.64	73.20	73.91	25.60

Table 9: To test whether there is a significant difference between DSVM result and the rest models for Flevoland (*significant at $p < 0.05$ or $t > |1.96|$)

Model	Lower confidence bound $[X_m - Y_m]$	Upper confidence bound $[X_m - Y_m]$	tstat	Standard deviation	P value
SVM	24.8808	25.0326	2.8362	0.0306	*0.0053
DNN	2.7521	3.0346	-1.9960	0.0569	*0.0482
GMM	23.9336	24.2998	3.8094	0.0737	*0.0002
KNN	23.2129	23.4137	3.8439	0.0404	*0.0002
KM	77.5528	77.9472	13.0373	0.0794	*0.0000

Table 10: To test whether there is a significant difference between DSVM result and the rest models for Winnipeg (*significant at $p < 0.05$ or $t > |1.96|$).

Model	Lower confidence bound $[X_m - Y_m]$	Upper confidence bound $[X_m - Y_m]$	tstat	Standard deviation	P value
SVM	25.7449	26.0484	2.9737	0.0611	*0.0035
DNN	2.9550	3.2783	-2.2109	0.0651	*0.0289
GMM	25.5103	25.6097	3.8800	0.0200	*0.0002
KNN	24.6604	25.0129	3.8898	0.0709	*0.0002
KM	72.9911	73.2822	12.7858	0.0586	*0.0000

Table 7 showed the results of the comparison between the DSVM and SVM models. The DSVM and SVM results for ERBF, GRBF, neural, and polynomial kernels for Flevoland were 99.17 (73.39), 99.32 (74.62), 98.64 (71.28), and 99.34 (77.21); while the DSVM and SVM results for ERBF, GRBF, neural, and polynomial kernels for Winnipeg were 98.65 (72.68), 98.67 (73.54), 98.27 (70.15), and 99.46 (75.03). The SVM results are the results in parenthesis. The SVM and DSVM results given in Table 5 showed that the DSVM outperformed the SVM. The DSVM was compared to other classifiers as depicted in Figures 20 and 21. Given in Table 8 was a summary of the classification accuracies of the DSVM, SVM, DNN, GMM, KNN, and KM classifiers. The results for DSVM, SVM, DNN, GMM, KNN, and KM classifiers for Flevoland were 99.12, 74.13, 96.29, 75.06, 75.85, and 21.43 respectively; while the results for DSVM, SVM, DNN, GMM, KNN, and KM classifiers for Winnipeg were 98.76, 72.85, 95.64, 73.20, 73.91, and 25.60 respectively. From Table 8, the comparison of the DSVM with other classifiers showed that the DSVM outperformed the SVM, DNN, GMM, KNN, and KM classifiers; while the DSVM and DNN results were close. This comparison was necessary since the GMM and KNN are conventional supervised classifiers while the KNN is a conventional unsupervised classifier. The KNN yielded the lowest classification accuracy while the DSVM yielded the highest classification accuracy.

Table 11: The computed Kappa coefficients of the DSVM, SVM, DNN, GMM, KNN, and KM models.

Images	Classifiers					
	DSVM	SVM	DNN	GMM	KNN	KM
Flevoland	0.92	0.70	0.88	0.68	0.68	0.18
Winnipeg	0.91	0.69	0.86	0.65	0.67	0.20

Tables 9 and 10 showed a student's t test to test whether there is a significant difference between the mean X_m of the DSVM results and the mean Y_m rest of the models based on a two-tailed test at the 95% confidence level for Flevoland and Winnipeg images. The null hypothesis H_0 was that $X_m = Y_m$; while the alternative hypothesis H_1 was that $X_m \neq Y_m$. We will reject H_0 when $t > |1.96|$. The results of the test for the Flevoland and Winnipeg showed that there were significant difference between the DSVM and the rest models' results. The computed Kappa coefficients for the DSVM, SVM, DNN, GMM, KNN, and KM models for Flevoland were 92.45, 70.71, 88.76, 68.59, 68.62, and 18.89 respectively; while the computed Kappa coefficients for DSVM, SVM, DNN, GMM, KNN, and KM models for Winnipeg were 92.45, 70.71, 88.76, 68.59, 68.62, and 18.89 respectively (see Table 7). The computed Kappa coefficients corroborated the results presented in Table 6. It can be discerned that for both images the KM produced the lowest accuracy while the DSVM produced the highest accuracy.

4. Discussion and conclusion

We presented the novel application of DSVM to PolSAR image classification. PolSAR imaging recently is among the most advanced remote sensing data source (Ferreira *et al.*, 2021). They are capable of yielding high resolution remote sensing images that are not compromised by flight altitude and weather conditions, and they provide data about the object structure (Samat *et al.*, 2018). They are extensively used for land cover classification because of their capacity to monitor objects' structures (Salehi *et al.*, 2013; Gopal Singh *et al.*, 2021). Even though optical remote sensing images mainly serve as data source for land cover classification, contrary to optical images PolSAR images have been very attractive for being unaffected by cloud cover (Homayouni *et al.*, 2019; Parikh *et al.*, 2020). PolSAR images have tremendous applications in mapping numerous earth phenomena such as flooding, urban growth, deforestation, earthquake monitoring, monitoring of civil infrastructure stability e.g. bridges, and military surveillance. Land cover classification requires robust algorithms for both features selection and classification (Hänsch & Hellwich, 2018; Liu *et al.*, 2021; Pourshamsi *et al.*, 2021). The proper classification and interpretation of PolSAR images is crucial. The major challenge for geoscientists is the development of robust algorithms for the optimal classification of PolSAR images. Even though scientists have developed conventional classifiers such as KM, KNN, GMM, etc., the advent of modern non-parametric classifiers like ANN and SVM has relatively relegated these conventional classifiers to the background. Recently the fusion of DL and non-parametric classifiers has quickly outclassed the use of standalone non-parametric classifiers such as ANN and SVM. In recent times several DNN techniques have been developed and experimented for PolSAR image classification. Some of the notable DNN applications were presented in section one, outperformed those of the standalone ANN classifier. The fusion of DL and SVM has been applied to a few studies e.g. Chui *et al.* (2020),

Okwuashi & Ndehedehe (2020), Wang *et al.*, (2020) etc. This research therefore experimented for the first time the use of the DSVM for PolSAR image classification.

This experiment was performed using a fully polarized SAR image of Flevoland region in Netherlands, and a fully polarimetric UAVSAR system, over an agricultural area in Winnipeg, MB, Canada (see Figures 4 and 10). PolSAR images are corrupted and adapted by a signal dependent multiplicative noise known as speckle. This speckle, by degrading the level of quality and detail contained in the acquired images decreases our potentiality to interpret the image. Although PolSAR observations can provide land cover information regardless of weather conditions, this speckle significantly affects the potential for accurate classification. Speckle noise is a common degrading factor in active remote sensing. In this work, the speckle noise in the images was suppressed by applying a 5 X 5 window size Lee filter. Texture analysis is the next vital component of our PolSAR image analysis. Texture analysis is the description of characteristic of the image properties by textural features (Guo *et al.*, 2020; Liao *et al.*, 2020; Garg & Garg, 2021). Texture is as a result of the local variations in brightness within a region of an image (Naseri *et al.*, 2012; Delibaş & Arslan, 2020; Szychot *et al.*, 2020; Farwell *et al.*, 2021). To extract the texture features from the PolSAR images the Pauli decomposition was used to decomposed the images into $|S_{HH} + S_{VV}|$, $|S_{HH} - S_{VV}|$, $|S_{HV}|$ polarimetric channels. The Pauli decomposition used in this work is a coherent decomposition method. Coherent and incoherent methods have their advantages and disadvantages. Coherent decomposition is usually suitable for analysing natural targets like water, vegetation etc., while incoherent decomposition is usually suitable for analysis man-made targets like buildings (Zhang *et al.*, 2008; Aghababae *et al.*, 2013; Parida & Mandal, 2020; Phartiyal *et al.*, 2020; Ramya & Kumar, 2021). In this experiment we chose the Pauli coherent decomposition method because it is expected to present a better distinction of the various vegetation classes and water.

Then the GLCM was computed from three polarimetric channels $|S_{HH} + S_{VV}|$, $|S_{HH} - S_{VV}|$, $|S_{HV}|$ based on correlation, contrast, energy, and homogeneity statistics. Four notable statistical texture features were used out of the numerous statistical texture features so as to reduce the dimension of the experimental data which is exponentially dimensionally large for efficient data processing and accuracy enhancement; and also to avoid the effect of “curse of dimensionality” (Bessa *et al.*, 2017; Aremu *et al.*, 2020; Hidalgo-Mompeán *et al.*, 2021) since the experimental data are exponentially dimensionally large. GLCM directions 0° , 45° , 90° , and 135° based on an offset distance of 60 were used to obtain these four statistics. GLCM are derived from second order textural features (see Figures 2b, 2c, 2d, and 2e). Textural statistical measures such as mean, median, standard deviation are first order textural features calculated from first order brightness values (e.g. as given in Figure 2a).

A strong correlation is expected for the computed directions 0° , 45° , 90° , and 135° (see Figures 8 and 14). In order to enhance the accuracy of our PolSAR classification we explored 8, 16, 32, 64, 128, and 256 quantization levels to compute for correlation, contrast, energy, and homogeneity for the Flevoland and Winnipeg images. The four statistics, correlation, contrast, energy, and homogeneity were extracted based on 8, 16, 32, 64, 128, and 256 quantization levels (see Figures 9 and 15). Quantization helps to improve the classification accuracy.

The main problem posed by PolSAR image classification is the ability to develop classifiers that can substantially separate the object classes present in the PolSAR image. To address this problem, this research explored a novel classification of PolSAR imagery using DSVM. DSVM is a hybrid algorithm achieved through a fusion of DL and the traditional SVM. DSVM basically consists of numerous connecting SVM weights (Okwuashi & Ndehedehe, 2020). The resulting statistical features for correlation, contrast, energy, and homogeneity were used to learn the DSVM for the classification of the two SAR images. Our hybrid DSVM is a composite of several SVMs. We employed four notable SVM kernels: ERBF, GRBF, neural, and polynomial. Both ERBF and GRBF have a free parameter called ‘gamma.’ This free gamma parameter is a common parameter that both kernels share. The neural kernel has two free parameters a and b ; while the polynomial kernel also has two free parameters c and d . The selection of the optimal model parameter values for ERBF, GRBF, neural, and polynomial kernels for the two images was done by ‘trial and error’ as shown in Figures 16 and 17. We also selected the optimal regularization parameter C for the four kernels as shown in Figures 18 and 19. The DSVM is abridged by individual SVMs representing the interconnecting weights of the network. The training of the network was based on the backpropagation technique. Therefore, instead of using one SVM to solve the problem, the problem was solved by several SVMs as expressed in Tables 3 and 4. Because the backpropagation technique is iterative, a loss function was used to ensure the convergence of the iteration. Tables 3 and 4 showed few results obtained from both images. The classification results of the two images with respect to the different land cover classes and kernel functions were shown in Tables 5 and 6. A comprehensive result of the DSVM with respect to the traditional SVM, DNN, GMM, KNN, and KM were shown in Table 8. The Student’s t test results for Flevoland and Winnipeg given in Tables 9 and 10 showed that there was significant difference between the DSVM result and those of the rest models at the 95% confidence level. This implied that the DSVM outperformed the rest model. For a fair assessment of the proposed DSVM model its results were compared with the conventional SVM. The DSVM was also compared with the known DNN. The DSVM results were also compared with the GMM and KNN being two renowned conventional supervised classifiers. The DSVM was also compared with the KM for it being one of the most common conventional unsupervised classifiers.

The accuracy of the models was also evaluated using the Kappa statistic or Kappa coefficient (see Table 11) (Cohen, 1960; Ma & Redmond, 1995; Lo & Yeung, 2007). Kappa coefficient measures the inter-rater reliability and the intra-rater reliability for qualitative items (Rajasekar *et al.*, 2017). The Kappa coefficient is assumed to be a more accurate measure than the usually used percent agreement calculation, due to the fact that it accounts for the agreement occurring by chance (Anderson & Delahanty, 2020; Duc *et al.*, 2021). According to Landis and Koch (1977) the Kappa results can be interpreted as follows: <0 (no agreement), 0.0 – 0.20 (slight agreement), 0.21– 0.40 (fair agreement), 0.41– 0.60 (moderate agreement), 0.61 – 0.80 (substantial agreement), 0.81 – 1.00 (almost perfect agreement). Therefore the computed Kappa coefficients presented in Table 11 can be interpreted as follows. The DSVM results for both Flevoland and Winnipeg images can be categorised as ‘almost perfect agreement.’ The SVM results for both Flevoland and Winnipeg images can be categorised as ‘substantial agreement.’ The DNN results for both Flevoland and Winnipeg images can be categorised as ‘almost perfect agreement.’ The GMM results for both Flevoland and Winnipeg images can be categorised as ‘substantial agreement.’ The KNN results for both Flevoland and Winnipeg images can be categorised as ‘substantial agreement.’ The KM results for both Flevoland and Winnipeg images can be categorised as ‘slight agreement.’ The classification results showed that the DSVM outperformed the rest classifiers. A closer look at the results revealed that the difference between the DSVM and DNN results was the lowest; nonetheless the difference between the DSVM result and the SVM result was high. The high difference between DSVM/DNN results and those of the conventional classifiers GMM, KNN, and KM was expected. DSVM applications are extremely few and still nascent. The result from this experiment had shown that the DSVM is a very robust hybrid model for PolSAR image classification. DL is relatively new and highly evolving. DL is basically associated with ANN, but in recent times there have been integrations of DL with the traditional SVM as experimented in this work. The result of this experiment has shown that the DSVM can yield a better result than the DNN.

Acknowledgement

This study received no external funding.

References

- Aghababae, H., Amini, J., & Tzeng, Y. C. (2013). Contextual PolSAR image classification using fractal dimension and support vector machines. *European Journal of Remote Sensing*, 46(1), 317-332.
- Ahishali, M., Kiranyaz, S., Ince, T., & Gabbouj, M. (2021). Classification of polarimetric SAR images using compact convolutional neural networks. *GIScience & Remote Sensing*, 58(1), 28-47.
- Alberga, V., Satalino, G., & Staykova, D. K. (2008). Comparison of polarimetric SAR observables in terms of classification performance. *International Journal of Remote Sensing*, 29(14), 4129-4150.
- An, W., Xie, C., Yuan, X., Cui, Y., & Yang, J. (2011). Four-component decomposition of polarimetric SAR images with deorientation. *IEEE Geoscience and Remote Sensing Letters*, 8(6), 1090-1094.
- Anderson, R. E., & Delahanty, D. L. (2020). Discrepant responding across measures of college students' sexual victimization experiences: Conceptual replication and extension. *The Journal of Sex Research*, 57(5), 585-596.
- Araujo, L. N., Belotti, J. T., Alves, T. A., de Souza Tadano, Y., & Siqueira, H. (2020). Ensemble method based on Artificial Neural Networks to estimate air pollution health risks. *Environmental Modelling & Software*, 123, 104567.
- Aremu, O. O., Hyland-Wood, D., & McAree, P. R. (2020). A machine learning approach to circumventing the curse of dimensionality in discontinuous time series machine data. *Reliability Engineering & System Safety*, 195, 106706.
- Attarchi, S. (2020). Extracting impervious surfaces from full polarimetric SAR images in different urban areas. *International Journal of Remote Sensing*, 41(12), 4644-4663.
- Bessa, M.A., Bostanabad, R., Liu, Z., Hu, A., Apley, D.W., Brinson, C., Chen, W., & Liu, W.K. (2017). A framework for data-driven analysis of materials under uncertainty: Countering the curse of dimensionality. *Computer Methods in Applied Mechanics and Engineering*, 320, 633-667.
- Boulila, W., Sellami, M., Driss, M., Al-Sarem, M., Safaei, M., & Ghaleb, F. A. (2021). RS-DCNN: A novel distributed convolutional-neural-networks based-approach for big remote-sensing image classification. *Computers and Electronics in Agriculture*, 182, 106014.
- Chen, S. W., Li, Y. Z., Wang, X. S., Xiao, S. P., & Sato, M. (2014). Modelling and interpretation of scattering mechanisms in polarimetric synthetic aperture radar: Advances and perspectives. *IEEE Signal Processing Magazine*, 31(4), 79-89.
- Chen, S. W., & Tao, C. S. (2018). PolSAR image classification using polarimetric-feature-driven deep convolutional neural network. *IEEE Geoscience and Remote Sensing Letters*, 15(4), 627-631.

- Chui, K. T., Liu, R. W., Zhao, M., & De Pablos, P. O. (2020). Predicting students' performance with school and family tutoring using generative adversarial network-based deep support vector machine. *IEEE Access*, 8, 86745-86752.
- Coelho, D. F., Cintra, R. J., Frery, A. C., & Dimitrov, V. S. (2018). Fast matrix inversion and determinant computation for polarimetric synthetic aperture radar. *Computers & Geosciences*, 119, 109-114.
- Cohen, J. (1960). A coefficient of agreement for nominal scales. *Educational and psychological measurement*, 20(1), 37-46.
- Cortes, C., & Vapnik, V. (1995). Support-vector networks. *Machine learning*, 20(3), 273-297.
- Delibaş, E., & Arslan, A. (2020). DNA sequence similarity analysis using image texture analysis based on first-order statistics. *Journal of Molecular Graphics and Modelling*, 107603.
- Del Frate, F., Schiavon, G., Solimini, D., Borgeaud, M., Hoekman, D. H., & Vissers, M. A. (2003). Crop classification using multiconfiguration C-band SAR data. *IEEE Transactions on Geoscience and Remote Sensing*, 41(7), 1611-1619.
- Du, P., Samat, A., Waske, B., Liu, S., & Li, Z. (2015). Random forest and rotation forest for fully polarized SAR image classification using polarimetric and spatial features. *ISPRS Journal of Photogrammetry and Remote Sensing*, 105, 38-53.
- Duc, P. N. H., Torterotot, M., Samaran, F., White, P. R., Gérard, O., Adam, O., & Cazau, D. (2021). Assessing inter-annotator agreement from collaborative annotation campaign in marine bioacoustics. *Ecological Informatics*, 61, 101185.
- Farwell, L.S., Gudex-Cross, D., Anise, I.E., Bosch, M.J., Olah, A.M., Radeloff, V.C., Razenkova, E., Rogova, N., Silveira, E.M., Smith, M.M., & Pidgeon, A.M. (2021). Satellite image texture captures vegetation heterogeneity and explains patterns of bird richness. *Remote Sensing of Environment*, 253, 112175.
- Ferreira, J. A., Coelho, H., & Nascimento, A. D. (2021). A family of divergence-based classifiers for Polarimetric Synthetic Aperture Radar (PolSAR) imagery vector and matrix features. *International Journal of Remote Sensing*, 42(4), 1201-1229.
- Fränti, P., & Sieranoja, S. (2018). K-means properties on six clustering benchmark datasets. *Applied Intelligence*, 48(12), 4743-4759.
- Frost, V. S., Stiles, J. A., Shanmugan, K. S., & Holtzman, J. C. (1982). A model for radar images and its application to adaptive digital filtering of multiplicative noise. *IEEE Transactions on pattern analysis and machine intelligence*, (2), 157-166.
- Fukuda, S., & Hirokawa, H. (2001). Polarimetric SAR image classification using support vector machines. *IEICE Transactions on Electronics*, 84(12), 1939-1945.
- Gadhiya, T., & Roy, A. K. (2019). Superpixel-Driven Optimized Wishart Network for Fast PolSAR Image Classification Using Global k -Means Algorithm. *IEEE Transactions on Geoscience and Remote Sensing*, 58(1), 97-109.
- Garg, P. K., & Garg, R. D. (2021). Texture-Based Riverine Feature Extraction and Flood Mapping Using Satellite Images. *Advances in Remote Sensing for Natural Resource Monitoring*, 405-430.
- Geng, J., Wang, H., Fan, J., & Ma, X. (2017). Deep supervised and contractive neural network for SAR image classification. *IEEE Transactions on Geoscience and Remote Sensing*, 55(4), 2442-2459.
- Gonzales, R. C., & Woods, R. E. (2002). *Digital image processing*. Addison-Wesley Publishing Company.
- Gonzalez, R. C., & Woods, R. E. (2008). *Digital Image Processing*, 3rd Edition 461-520.
- Gao, W., Yang, J., & Ma, W. (2014). Land cover classification for polarimetric SAR images based on mixture models. *Remote Sensing*, 6(5), 3770-3790.
- Gopal Singh, P., Bordu, N., Singh, D., Yahia, H., & Daoudi, K. (2021). Permuted Spectral and Permuted Spectral-Spatial CNN Models for PolSAR-Multispectral Data based Land Cover Classification. *International Journal of Remote Sensing*, 42(3), 1096-1120.
- Gui, R., Xu, X., Yang, R., Xu, Z., Wang, L., & Pu, F. (2021). A General Feature Paradigm for Unsupervised Cross-Domain PolSAR Image Classification. *IEEE Geoscience and Remote Sensing Letters*.
- Guo, W., Rees, G., & Hofgaard, A. (2020). Delineation of the forest-tundra ecotone using texture-based classification of satellite imagery. *International Journal of Remote Sensing*, 41(16), 6384-6408.
- Guyon, I., Weston, J., Barnhill, S., & Vapnik, V. (2002). Gene selection for cancer classification using support vector machines. *Machine learning*, 46(1), 389-422.
- Han, P., Han, B., Lu, X., Cong, R., & Sun, D. (2020). Unsupervised classification for PolSAR images based on multi-level feature extraction. *International Journal of Remote Sensing*, 41(2), 534-548.
- Hänsch, R., & Hellwich, O. (2018). Skipping the real world: Classification of PolSAR images without explicit feature extraction. *ISPRS Journal of Photogrammetry and Remote Sensing*, 140, 122-132.
- Hara, Y., Atkins, R. G., Yueh, S. H., Shin, R. T., & Kong, J. A. (1994). Application of neural networks to radar image classification. *IEEE Transactions on Geoscience and Remote Sensing*, 32(1), 100-109.
- Haralick, R. M., Shanmugam, K., & Dinstein, I. H. (1973). Textural features for image classification. *IEEE Transactions on systems, man, and cybernetics*, (6), 610-621.

- Hidalgo-Mompeán, F., Fernández, J. F. G., Cerruela-García, G., & Márquez, A. C. (2021). Dimensionality analysis in machine learning failure detection models. A case study with LNG compressors. *Computers in Industry*, 128, 103434.
- Homayouni, S., McNairn, H., Hosseini, M., Jiao, X., & Powers, J. (2019). Quad and compact multitemporal C-band PolSAR observations for crop characterization and monitoring. *International Journal of Applied Earth Observation and Geoinformation*, 74, 78-87.
- Imani, M. (2021). A random patches based edge preserving network for land cover classification using Polarimetric Synthetic Aperture Radar images. *International Journal of Remote Sensing*, 42(13), 4946-4964.
- Jain, A. K. (1989). Fundamentals of digital image processing. Englewood Cliffs, NJ: Prentice Hall, 1st ed.
- Joel, T., & Sivakumar, R. (2013). Despeckling of ultrasound medical images: A survey. *Journal of Image and Graphics*, 1(3), 161-165.
- Khan, S. U., Islam, N., Jan, Z., Haseeb, K., Shah, S. I. A., & Hanif, M. (2021). A machine learning-based approach for the segmentation and classification of malignant cells in breast cytology images using gray level co-occurrence matrix (GLCM) and support vector machine (SVM). *Neural Computing and Applications*, 1-8.
- Khojastehnazhand, M., & Ramezani, H. (2020). Machine vision system for classification of bulk raisins using texture features. *Journal of Food Engineering*, 271, 109864.
- Kotsiopoulos, T., Sarigiannidis, P., Ioannidis, D., & Tzovaras, D. (2021). Machine Learning and Deep Learning in smart manufacturing: The Smart Grid paradigm. *Computer Science Review*, 40, 100341.
- Kourgli, A., Ouarzeddine, M., Oukil, Y., & Belhadj-Aissa, A. (2012). Texture modelling for land cover classification of fully polarimetric SAR images. *International Journal of Image and Data Fusion*, 3(2), 129-148.
- Kuan, D. T., Sawchuk, A. A., Strand, T. C., & Chavel, P. (1985). Adaptive noise smoothing filter for images with signal-dependent noise. *IEEE transactions on pattern analysis and machine intelligence*, (2), 165-177.
- Kupidura, P. (2019). The Comparison of different methods of texture analysis for their efficacy for land use classification in satellite imagery. *Remote Sensing*, 11(10), 1233.
- Landis, J. R., & Koch, G. G. (1977). The measurement of observer agreement for categorical data. *biometrics*, 159-174.
- Lee, J. S. (1980). Digital image enhancement and noise filtering by use of local statistics. *IEEE transactions on pattern analysis and machine intelligence*, (2), 165-168.
- Lee, J. S. (1981). Refined filtering of image noise using local statistics. *Computer graphics and image processing*, 15(4), 380-389.
- Liao, Z., He, B., & Quan, X. (2020). Potential of texture from SAR tomographic images for forest aboveground biomass estimation. *International Journal of Applied Earth Observation and Geoinformation*, 88, 102049.
- Linka, K., Hillgärtner, M., Abdolazizi, K. P., Aydin, R. C., Itskov, M., & Cyron, C. J. (2021). Constitutive artificial neural networks: A fast and general approach to predictive data-driven constitutive modeling by deep learning. *Journal of Computational Physics*, 429, 110010.
- Liu, D., Qi, Z., Zhang, H., Li, X., Yeh, A. G. O., & Wang, J. (2021). Investigation of the capability of multitemporal RADARSAT-2 fully polarimetric SAR images for land cover classification: a case of Panyu, Guangdong province. *European Journal of Remote Sensing*, 54(1), 338-350.
- Liu, F., Jiao, L., Tang, X., Yang, S., Ma, W., & Hou, B. (2018). Local restricted convolutional neural network for change detection in polarimetric SAR images. *IEEE transactions on neural networks and learning systems*, 30(3), 818-833.
- Lo, C. P. & Yeung, A. K. W. (Eds.) (2007). *Concepts and techniques of geographic information systems* (2nd ed.), Upper Saddle River, NJ: Pearson Prentice Hall.
- Loupas, T., McDicken, W. N., & Allan, P. L. (1989). An adaptive weighted median filter for speckle suppression in medical ultrasonic images. *IEEE transactions on Circuits and Systems*, 36(1), 129-135.
- Lussier, F., Thibault, V., Charron, B., Wallace, G. Q., & Masson, J. F. (2020). Deep learning and artificial intelligence methods for Raman and surface-enhanced Raman scattering. *TrAC Trends in Analytical Chemistry*, 124, 115796.
- Ma, Y., Li, Y., & Zhu, L. (2019). Land Cover Classification for Polarimetric SAR Image Using Convolutional Neural Network and Superpixel. *Progress In Electromagnetics Research*, 83, 111-128.
- Ma, Z., & Redmond, R. L. (1995). Tau coefficients for accuracy assessment of classification of remote sensing data. *Photogrammetric Engineering and Remote Sensing*, 61(4), 435-439.
- Mahdianpari, M., Motagh, M., Akbari, V., Mohammadimanesh, F., & Salehi, B. (2019). A Gaussian random field model for de-speckling of multi-polarized Synthetic Aperture Radar data. *Advances in Space Research*, 64(1), 64-78.
- Mahdianpari, M., Salehi, B., Mohammadimanesh, F., Brisco, B., Mahdavi, S., Amani, M., & Granger, J. E. (2018). Fisher Linear Discriminant Analysis of coherency matrix for wetland classification using PolSAR imagery. *Remote Sensing of Environment*, 206, 300-317.

- Marr, D., & Hildreth, E. (1980). Theory of edge detection. *Proceedings of the Royal Society of London. Series B. Biological Sciences*, 207(1167), 187-217.
- Maulik, U., & Chakraborty, D. (2017). Remote Sensing Image Classification: A survey of support-vector-machine-based advanced techniques. *IEEE Geoscience and Remote Sensing Magazine*, 5(1), 33-52.
- McNairn, H., Shang, J., Jiao, X., & Champagne, C. (2009). The contribution of ALOS PALSAR multipolarization and polarimetric data to crop classification. *IEEE Transactions on Geoscience and Remote Sensing*, 47(12), 3981-3992.
- Mering, C., & Chopin, F. (2002). Granulometric maps from high resolution satellite images. *Image Analysis & Stereology*, 21(1), 19-24.
- Milošević, D., Milosavljević, A., Predić, B., Medeiros, A. S., Savić-Zdravković, D., Piperac, M. S., Kostić, T., Spasić, F., & Leese, F. (2020). Application of deep learning in aquatic bioassessment: Towards automated identification of non-biting midges. *Science of the Total Environment*, 711, 135160.
- Mullissa, A. G., Persello, C., & Reiche, J. (2021). Despeckling Polarimetric SAR Data Using a Multistream Complex-Valued Fully Convolutional Network. *IEEE Geoscience and Remote Sensing Letters*.
- Naseri, A., Pouyan, A., & Kavian, N. (2012). Automatic Detection of Retina Layers using Texture Analysis. *International Journal of Computer Applications*, 46(1), 29-33.
- Nguyen, H. H., Cho, S., Jeong, J., & Choi, M. (2021). A D-vine copula quantile regression approach for soil moisture retrieval from dual polarimetric SAR Sentinel-1 over vegetated terrains. *Remote Sensing of Environment*, 255, 112283.
- Numbisi, F. N., Van Coillie, F., & De Wulf, R. (2019). Delineation of cocoa agroforests using multiseason Sentinel-1 SAR images: a low grey level range reduces uncertainties in GLCM texture-based mapping. *ISPRS International Journal of Geo-Information*, 8(4), 179.
- Okwuashi, O., & Ndehedehe, C. (2017). Tide modelling using support vector machine regression. *Journal of Spatial Science*, 62(1), 29-46.
- Okwuashi, O., & Ndehedehe, C. E. (2020). Deep support vector machine for hyperspectral image classification. *Pattern Recognition*, 107298.
- Özcan, C., Ersoy, K. O., & Oğul, İ. Ü. (2020). Fast texture classification of denoised SAR image patches using GLCM on Spark. *Turkish Journal of Electrical Engineering & Computer Sciences*, 28(1), 182-195.
- Parida, B. R., & Mandal, S. P. (2020). Polarimetric decomposition methods for LULC mapping using ALOS L-band PolSAR data in Western parts of Mizoram, Northeast India. *SN Applied Sciences*, 2, 1-15.
- Parikh, H., Patel, S., & Patel, V. (2020). Classification of SAR and PolSAR images using deep learning: a review. *International Journal of Image and Data Fusion*, 11(1), 1-32.
- Phartiyal, G. S., Kumar, K., & Singh, D. (2020). An improved land cover classification using polarization signatures for PALSAR 2 data. *Advances in Space Research*, 65(11), 2622-2635.
- Pirra, M., & Diana, M. (2019). A study of tour-based mode choice based on a support vector machine classifier. *Transportation Planning and Technology*, 42(1), 23-36.
- Ponnurangam, G. G., & Rao, Y. S. (2018). The application of compact polarimetric decomposition algorithms to L-band PolSAR data in agricultural areas. *International Journal of Remote Sensing*, 39(22), 8337-8360.
- Pourshamsi, M., Xia, J., Yokoya, N., Garcia, M., Laval, M., Pottier, E., & Balzter, H. (2021). Tropical forest canopy height estimation from combined polarimetric SAR and LiDAR using machine-learning. *ISPRS Journal of Photogrammetry and Remote Sensing*, 172, 79-94.
- Rajasekar, S., Banger, R. K., & Sekaran, P. (2017). Inter-rater and intra-rater reliability of a movement control test in shoulder. *Journal of bodywork and movement therapies*, 21(3), 739-742.
- Ramya, M. N. S., & Kumar, S. (2021). PolInSAR coherence-based decomposition modelling for scattering characterization: A case study in Uttarakhand, India. *Science of Remote Sensing*, 3, 100020.
- Reisi-Gahrouei, O., Homayouni, S., McNairn, H., Hosseini, M., & Safari, A. (2019). Crop biomass estimation using multi regression analysis and neural networks from multitemporal L-band polarimetric synthetic aperture radar data. *International Journal of Remote Sensing*, 40(17), 6822-6840.
- Richardson, A., Goodenough, D. G., Chen, H., Moa, B., Hobart, G., & Myrvold, W. (2010, July). Unsupervised nonparametric classification of polarimetric SAR data using the K-nearest neighbor graph. In *2010 IEEE International Geoscience and Remote Sensing Symposium* (pp. 1867-1870). IEEE.
- Rollet, R., Benie, G. B., Li, W., Wang, S., & Boucher, J. M. (1998). Image classification algorithm based on the RBF neural network and K-means. *International Journal of Remote Sensing*, 19(15), 3003-3009.
- Rostami, O., & Kaveh, M. (2021). Optimal feature selection for SAR image classification using biogeography-based optimization (BBO), artificial bee colony (ABC) and support vector machine (SVM): a combined approach of optimization and machine learning. *Computational Geosciences*, 1-20.
- Salazar, D.F., Demattê, J.A., Vicente, L.E., Guimarães, C.C., Sayão, V.M., Cerri, C.E., Padilha, M.C.D.C., & Mendes, W. (2020). Emissivity of agricultural soil attributes in southeastern Brazil via terrestrial and satellite sensors. *Geoderma*, 361, 114038.

- Salehi, M., Sahebi, M. R., & Maghsoudi, Y. (2013). Improving the accuracy of urban land cover classification using Radarsat-2 PolSAR data. *IEEE Journal of selected topics in applied Earth Observations and Remote Sensing*, 7(4), 1394-1401.
- Samat, A., Gamba, P., Liu, S., Miao, Z., Li, E., & Abuduwaili, J. (2018). Quad-PolSAR data classification using modified random forest algorithms to map halophytic plants in arid areas. *International journal of applied earth observation and geoinformation*, 73, 503-521.
- Shang, F., Kishi, N., & Hirose, A. (2019). Degree of polarization-based data filter for fully polarimetric synthetic aperture radar. *IEEE Transactions on Geoscience and Remote Sensing*, 57(6), 3767-3777.
- Shang, R., He, J., Wang, J., Xu, K., Jiao, L., & Stolkin, R. (2020). Dense connection and depthwise separable convolution based CNN for polarimetric SAR image classification. *Knowledge-Based Systems*, 105542.
- Shao, Y., Cheng, Y., Shah, R. U., Weir, C. R., Bray, B. E., & Zeng-Treitler, Q. (2021). Shedding Light on the Black Box: Explaining Deep Neural Network Prediction of Clinical Outcomes. *Journal of Medical Systems*, 45(1), 1-9.
- Shen, H., Lin, L., Li, J., Yuan, Q., & Zhao, L. (2020). A residual convolutional neural network for polarimetric SAR image super-resolution. *ISPRS Journal of Photogrammetry and Remote Sensing*, 161, 90-108.
- Shi, H., Zhao, L., Yang, J., Lopez-Sanchez, J.M., Zhao, J., Sun, W., Shi, L., & Li, P., (2021). Soil moisture retrieval over agricultural fields from L-band multi-incidence and multitemporal PolSAR observations using polarimetric decomposition techniques. *Remote Sensing of Environment*, 261, 112485.
- Soh, L. K., & Tsatsoulis, C. (1999). Texture analysis of SAR sea ice imagery using gray level co-occurrence matrices. *IEEE Transactions on geoscience and remote sensing*, 37(2), 780-795.
- Sui, H., An, K., Xu, C., Liu, J., & Feng, W. (2018). Flood detection in PolSAR images based on level set method considering prior geoinformation. *IEEE Geoscience and Remote Sensing Letters*, 15(5), 699-703.
- Tavallali, P., Tavallali, P., & Singhal, M. (2021). K-means tree: an optimal clustering tree for unsupervised learning. *The Journal of Supercomputing*, 77(5), 5239-5266.
- Wang, C., Su, W., & Gu, H. (2021). A joint change detection method on complex-valued polarimetric synthetic aperture radar images based on feature fusion and similarity learning. *International Journal of Remote Sensing*, 42(13), 4864-4881.
- Wang, P., Qiao, H., Zhang, Y., Li, Y., Feng, Q., & Chen, K. (2020). Meso-damage evolution analysis of magnesium oxychloride cement concrete based on X-CT and grey-level co-occurrence matrix. *Construction and Building Materials*, 255, 119373.
- Waske, B., & Braun, M. (2009). Classifier ensembles for land cover mapping using multitemporal SAR imagery. *ISPRS Journal of Photogrammetry and Remote Sensing*, 64(5), 450-457.
- Wei, B., Yu, J., Wang, C., Wu, H., & Li, J. (2014). PolSAR image classification using a semi-supervised classifier based on hypergraph learning. *Remote sensing letters*, 5(4), 386-395.
- Wiener, N. (1949). Extrapolation, Interpolation and Smoothing of Stationary. *Time Series, with Engineering Applications*.
- Wurm, M., Taubenböck, H., Weigand, M., & Schmitt, A. (2017). Slum mapping in polarimetric SAR data using spatial features. *Remote sensing of environment*, 194, 190-204.
- Xia, J., Yang, X., & Jia, L. (2018). A multi-depth convolutional neural network for SAR image classification. *Remote sensing letters*, 9(12), 1138-1147.
- Yahia, M., Ali, T., Mortula, M. M., Abdelfattah, R., & Elmahdy, S. (2021). Polarimetric SAR Image Filtering by Infinite Number of Looks Prediction Technique. *IEEE Journal of Selected Topics in Applied Earth Observations and Remote Sensing*, 14, 4167-4184.
- Zendehboudi, A., Baseer, M. A., & Saidur, R. (2018). Application of support vector machine models for forecasting solar and wind energy resources: A review. *Journal of cleaner production*, 199, 272-285.
- Zhai, W., Zhang, J., Xiao, X., Wang, J., Zhang, H., Yin, X., & Wu, Z. (2021). Damaged building extraction from post-earthquake PolSAR data based on the Fourier transform. *Remote Sensing Letters*, 12(6), 594-603.
- Zhang, J., Zhang, J., & Zhao, Z. (2018). Study on the Classification of Gaofen-3 Polarimetric SAR Images Using Deep Neural Network. *Int. Arch. Photogramm. Remote Sens. Spat. Inf. Sci.*, 42, 2263-2266.
- Zhang, L., Zhang, J., Zou, B., & Zhang, Y. (2008). Comparison of methods for target detection and applications using polarimetric SAR image. *Piers online*, 4(1), 140-145.
- Zhang, P., Qian, X., Guo, X., Yang, X., & Li, G. (2020). Automated demarcation of the homogeneous domains of trace distribution within a rock mass based on GLCM and ISODATA. *International Journal of Rock Mechanics and Mining Sciences*, 128, 104249.
- Zhou, Y., Wang, H., Xu, F., & Jin, Y. Q. (2016). Polarimetric SAR image classification using deep convolutional neural networks. *IEEE Geoscience and Remote Sensing Letters*, 13(12), 1935-1939.

